THEORETICAL STUDIES OF TRANSITION METAL SURFACES AS ELECTROCATALYSTS FOR OXYGEN ELECTROREDUCTION

A Dissertation

by

EDUARDO J. LAMAS

Submitted to the Office of Graduate Studies of
Texas A&M University
in partial fulfillment of the requirements for the degree of

DOCTOR OF PHILOSOPHY

May 2007

Major Subject: Chemical Engineering

THEORETICAL STUDIES OF TRANSITION METAL SURFACES AS ELECTROCATALYSTS FOR OXYGEN ELECTROREDUCTION

A Dissertation

by

EDUARDO J. LAMAS

Submitted to the Office of Graduate Studies of
Texas A&M University
in partial fulfillment of the requirements for the degree of

DOCTOR OF PHILOSOPHY

Approved by:

Chair of Committee,	Perla B. Balbuena
Committee Members,	A. John Appleby
	Tahir Cagin
	Michael B. Hall
Head of Department,	N. K. Anand

May 2007

Major Subject: Chemical Engineering

.

ABSTRACT

Theoretical Studies of Transition Metal Surfaces as Electrocatalysts for Oxygen Electroreduction. (May 2007)

Eduardo J. Lamas B.S., Universidad de Buenos Aires
Chair of Advisory Committee: Dr. Perla B. Balbuena

In the last few years the quest towards a hydrogen based economy has intensified interest for effective and less expensive catalysts for fuel cell applications. Due to its slow kinetics, alternative catalysts for the oxygen electroreduction reaction are actively researched. Platinum alloys with different transition metals (for example: Ni, Co and Fe) have shown improved activity over pure Pt. The design of a Pt-free catalysts is also highly desirable, and different alternatives including metalloporphyrins and Pd-based catalysts are being researched. Pd-based catalysts constitute an attractive alternative to Pt alloys in some fuel cell applications, not only because of lower costs but also because of the lower reactivity of Pt alloys towards methanol, which is important for improved methanol crossover tolerance on direct methanol fuel cells.

In this work we apply density functional theory (DFT) to the study of four catalysts for oxygen electroreduction. The electronic structure of these surfaces is characterized together with their surface reconstruction properties and their interactions with oxygen electroreduction intermediates both in presence and absence of water. The energetics obtained for the intermediates is combined with entropy data from thermodynamic tables to generate free energy profiles for two representative reaction mechanisms where the cell potential is included as a variable. The study of the barriers in these profiles points to the elementary steps in the reaction mechanisms that are likely to be rate-determining. The highest barrier in the series pathway is located at the first proton and charge transfer on all four catalytic surfaces. This is in good agreement with observed rate laws for this reaction. The instability of hydrogen peroxide on all surfaces, especially compared with the relatively higher stability of other intermediates, strongly points at this intermediate

as the most likely point where the oxygen bond is broken during oxygen reduction. This adds to the argument that this path might be active during oxygen electroreduction.

A better understanding behind the reaction mechanism and reactivities on these representative surfaces will help to find systematic ways of improvement of currently used catalysts in the oxygen electroreduction reaction.

A la memoria de mi Papá, para mi Mamá,
mi hermana y la pequeña Lulú

para mi Tía Beba y mis primos Lionel, Eric y Silvina

ACKNOWLEDGEMENTS

I wish to thank John Appleby for his insight on this topic and his many suggestions which were invaluable in helping me to improve this work.

During these years, I have encountered many good people and I would also like to express my gratitude to them.

Finally, I wish to thank my professors at the University of Buenos Aires for the work they do, most of the time with no other resources than their talent and imagination.

TABLE OF CONTENTS

.

Page

LIST OF FIGURES

Page

.

Page

.

.

LIST OF TABLES

.

.

1. INTRODUCTION

When I read it, I don't wince, which is all I ever ask for a
book I write.
- Norman Mailer

Catalysts have been used in industry to improve speed and selectivity of chemical transformations to obtain either energy or more valuable chemicals (or both, as in the case of modern highly energy-integrated chemical processes) for many years, and their design and preparations is an industry in itself. The origin of the word catalyst is attributed to Jöns Jakob Berzelius, one of the founding fathers of chemistry and the person who developed modern chemical notation; Berzelius observed in 1835 that the hydrolysis of starch proceeded faster in malt diastase than in sulfuric acid. During most part of the chemical engineering history and since the observation and identification of the first catalytic reactions, the task of catalyst selection remained more of an art than a science. Nowadays, the existence of better experimental characterization techniques and the use of theoretical tools are helping to close this gap between art and science, allowing more systematic approaches to catalyst design. The understanding of physical causes behind improvement or deficiencies in a catalyst provides the engineer with a systematic and efficient route to its improvement.

The continuum increase of computer power together with the advancement of parallel algorithms that can efficiently solve Schrödinger's equation on systems that were considered out of reach just few years ago gives the researcher a variety of theoretical tools to model catalytic reactions. The understanding of the tools employed, and their strengths and limitations is crucial. One of the most obvious advantages of simulations over experimental techniques lies on the perfect controllability that the theoretical experiment has to offer. A single characteristic and its effects in the outcome of a complex process can be isolated and studied. For example, the effects of surface relaxation, band structure, presence of a solvent or second component distribution in an

---

This dissertation follows the style of Electrochimica Acta.

.

alloy in adsorption energies can be isolated, allowing us to identify the most important features without getting lost in the details. On the other hand, models are based in assumptions and simplifications that sometimes are limited. Their failure to describe some properties or systems, or systems sizes and temporal scales that can be efficiently handled, remain a limitation. That is why a reality check of results obtained is always necessary. We can give many case examples where density functional theory fails to provide the right answer to certain common physical problems. Among these the inability of DFT to correctly predict the tail of the Lennard-Jones potential for long range interactions; its poor prediction of band gaps, and more specifically examples we may also mention a recent discussion concerning the incorrect preferred adsorption site for CO on transition metals[1-3], and problems describing π stacking. It also fails to predict the correct band structure of Mott insulators, for example, for FeO case and other materials. As a final and far less sophisticated example of the care required in preparing a model, lets us point to the simpler aspect of setting the unit cell size when the adlayer does not follow the periodicity of the substrate. If a cell size that correctly captures only the surface is used, this might induce fictitious stresses and enforce an unrealistic adsorbate distribution. Special care will have to be taken at interpreting the results obtained when working under these conditions. Succinctly, we have mentioned some points about the importance of the correct choice of initial set-ups and theoretical tools. It is also important to know their limitations to have a feeling for their accuracy. Different properties may be described by theoretical tools with different levels of success so establishing references with similar systems or, even better, the same system and experimental observations is a crucial task to achieve sound results. All electron atomization energies are widely available for a variety of functionals can be found in the references cited and a very complete library of calculations is available at the National Institute of Standards and Technology web site[4], including geometries, vibrational data, energies, etc.

The aim of this work is the analysis of four different possible transition metal catalysts for oxygen electroreduction. We will focus our analysis on Pt, Pd and their

.

alloys with Co. We will study their electronic structures, their surface relaxation behavior, their interaction with the different intermediates of oxygen electroreduction both in the presence and absence of water, and their reaction free energies profiles at different cell potentials.

Figure 1.1 shows a flow chart for a catalyst design based on theoretical grounds. As with most design processes it is iterative in nature and the result of each iteration cycle is fed to the next cycle with the intended objective of an improved design. This work is organized closely following the flow chart just discussed. The second section is devoted to an analysis of the theoretical tools used in our work we travel the path from the full Schrödinger equation to the one electron density functional theory (DFT) equation. At each stop in this path we review the assumptions, simplifications and their consequences. A correct understanding of the strengths and limitations electronic structure models is crucial for its successful application and the analysis of its results. In the third section we analyze the state of knowledge on the particular reaction we are studying: which catalysts are currently being used, which ones are believed to be the detrimental factors to catalytic performance, which characteristics have been attributed to be the key to catalyst enhancements, and which are the routes that must be taken in order to exploit these characteristics.

In the second part of this dissertation we present our results and analysis on the four different catalytic surfaces. Following Figure 1.1, we start with the simplest system, i.e., the clean (111) surfaces by calculating its most important characteristic that is the position of the d-band center and analyze its structure and structural behavior when adsorbed species are present. We continue with a complete analysis including all the oxygen electroreduction intermediates, first in the absence of water, and in a second iteration including the effects of water. In both cases, we built free energy profiles for two different possible mechanisms and analyze them. Finally, in Section 9 all the conclusions are summarized.

.

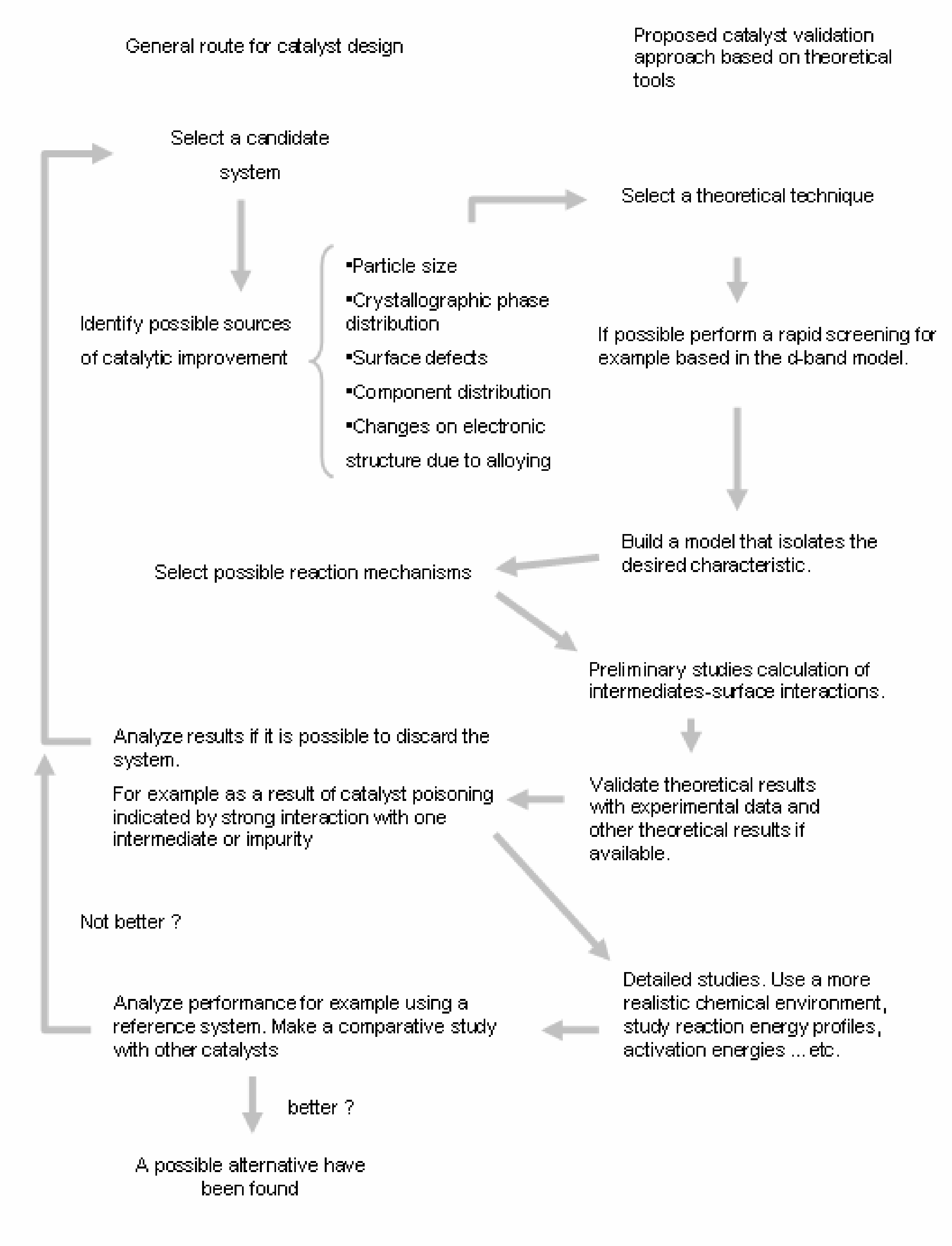

Fig. 1.1. General schematic route for catalyst design from a theoretical perspective.

2. ELECTRONIC STRUCTURE THEORY

> Had I ever known that we were not going to get rid of this damned quantum jumping, I never would have involved myself in this business!
>
> - Erwin Schrödinger

2.1. Introduction

In this section we will explore the theoretical grounds for the methods that later on will be repeatedly applied in this dissertation to the characterization of transition metal surfaces as electrocatalysts. The knowledge of the underlying theory is necessary not only for understanding the hypotheses used and how they influence the results but also their limitations so as to achieve a correct interpretation of the data obtained. The objective is not trivialize a deep, vast and complex theory, but to point out its key assumptions, mathematical tools, concepts and limitations in order to build a useful foundation for the rest of this work.

The all-electron Schrödinger equation for a generic multi-nuclei multi-electron system can be written as:

$$\hat{H}\cdot\left|\Phi\right\rangle = E\cdot\left|\Phi\right\rangle \tag{2.1}$$

where $\hat{H}$ is the system Hamiltonian with the following form:

$$\hat{H}(r_i,R_A) = \underbrace{-\sum_{i=1}^{N}\frac{1}{2}\nabla_i^2}_{(1)}\ \underbrace{-\sum_{A=1}^{M}\frac{1}{2\cdot M_A}\nabla_A^2}_{(2)}\ \underbrace{-\sum_{i=1}^{N}\sum_{A=1}^{M}\frac{Z_A}{\left|r_i-R_A\right|}}_{(3)}\ \underbrace{+\sum_{i=1}^{N}\sum_{j>i}^{N}\frac{1}{\left|r_i-r_j\right|}}_{(4)}\ \underbrace{+\sum_{A=1}^{M}\sum_{B>A}^{M}\frac{Z_A\cdot Z_B}{\left|R_A-R_B\right|}}_{(5)} \tag{2.2}$$

.

where the Hamiltonian components are:

(1) The kinetic energy of the electrons
(2) The kinetic energy of the nuclei
(3) The Coulombic interactions between the nuclei and the electrons
(4) The Coulombic interaction between the electrons
(5) The Coulombic interactions between the nuclei

In principle, the solution to this equation is all we need to characterize the chemistry of any given system but the complexity is at first glance overwhelming as Dirac famously stated in 1929 “The fundamental laws necessary for the mathematical treatment of a large part of physics and the whole of chemistry are thus completely known, and the difficulty lies only in the fact that application of these laws leads to equations that are too complex to be solved”. Despite his pessimism the advancement in theory (especially the development of Density Functional Theory and parallel algorithms) together with the amazing development of computing power, makes it possible to handle even relatively large systems.

Before analyzing the required simplifications to efficiently handle the original Hamiltonian in detail, we will summarize the key assumptions and mathematical techniques involved in the simplification and generation of a numerically tractable form of the Schrödinger equation, usually a one electron formulation:

- Born Oppenheimer Approximation (Section 2.2.1)
- Variational Principle for the Ground State (Section 2.2.2)
- Density Functional Theory (Section 2.2.3)
- Hilbert Spaces and the Schrödinger Equation (Section 2.2.4)
- DFT in Periodic Systems (Bloch’s condition) (Section 2.2.5)
- The Pseudopotential Approach (Section 2.2.6)

.

As we can see this entire simplification process can be reduced to a few key steps. However, the solution of the final equations is still a challenging task, although each step is conceptually clear. The implications of each of these simplifications on the quality of the solutions obtained should be discussed.

2.2. Simplifying Schrödinger's Equation

2.2.1. The Born Oppenheimer Approximation

Equation 1 shows the complexity of the pathway to finding a usable form of the Schrödinger equation allowing the handling of systems with more than a few electrons. We have on hand an apparently unsolvable problem, a complex partial differential equation with many coupled variables.

The main objective behind the Born Oppenheimer approximation is to decouple the electronic and ionic wave functions, thereby greatly simplifying Equation 2.1. The physical reason on why this decoupling is feasible is rooted in the different of masses of nuclei and electrons. This difference in masses (a proton is roughly 2000 times heavier than an electron) implies a difference of greater than two orders of magnitude in the kinetic energies of ions and electrons. It is therefore possible to assume that for each ionic position (for example when the atoms in a molecule or solid are vibrating) the electrons can instantly follow the nuclei due to their much faster dynamics adopting at each moment the corresponding ground state associated with fixed nuclear positions. This approximation is extensively used in quantum chemistry and physics calculations

The Born-Oppenheimer's approximation is based on the Born-Oppenheimer Ansatz. That is, we assume that the solution to the Schrödinger equation is of the form:

$$\Phi(\vec{r},\vec{R}) = \Psi(\vec{r},\vec{R}) \cdot \xi(\vec{R}) \qquad (2.3)$$

in which the system wave function is factored into an antisymmetric electronic wave function so it obeys the Pauli exclusion principle, $\Psi(\vec{r},\vec{R})$ where the nuclei coordinates

.

acts now as parameters and a nuclei wave function $\Phi(\vec{R})$. The clamped (fixed nuclei) electron equation is a solution of:

$$\hat{H} \cdot |\Psi\rangle = E \cdot |\Psi\rangle \tag{2.4}$$

where $\hat{H}$ is the system Hamiltonian with the following form:

$$\hat{H}(r_i, R_A) = \underbrace{-\sum_{i=1}^{N} \frac{1}{2} \nabla_i^2}_{(1)} \underbrace{- \sum_{i=1}^{N} \sum_{A=1}^{M} \frac{Z_A}{|r_i - R_A|}}_{(2)} + \underbrace{\sum_{i=1}^{N} \sum_{j>i}^{N} \frac{1}{|r_i - r_j|}}_{(3)} \tag{2.5}$$

where the Hamiltonian components are:

(1) Kinetic energy of the electrons
(2) Coulombic interactions between the nuclei and the electrons
(3) Coulombic interaction between the electrons

Despite being almost universally applied, examples were the approximation fails or corrections are necessary can be found in the literature. The interested reader is directed for example to extensive literature on electron phonon-interaction, where a good starting point are solid state physics text books, or to very accurate calculations of the energetics and vibrational frequencies of small molecules (see for example Handy et al[5]). In an extensive review, Butler[6] has discussed different reactions where a breakdown in the Born-Oppenheimer approximation is possible, and its consequences.

.

2.2.2. The Variational Principle

Perhaps the most important property is associated with the Schrödinger equation ground state. It states that if the energy is written as a functional of the wave function, i.e. a function that takes another function as its argument giving a real number as its return value, then the best ground state wavefunction is that giving a minimum in the energy functional. Mathematically the variational principle can be also expressed in the following way:

$$\left\langle E_{exact} \right\rangle = \left\langle \Psi_{exact} \middle| H \middle| \Psi_{exact} \right\rangle < \left\langle \Psi_{trial} \middle| H \middle| \Psi_{trial} \right\rangle = \left\langle E_{trial} \right\rangle \tag{2.6}$$

The variational principle is generally applied in two different ways. The first is used both in DFT and in the Hartree-Fock method. The closest possible solution in a subspace (see Section 2.2.4) spammed by a selected basis set is found by adjusting the parameters defining the resulting wavefunctions, i.e. those from the linear combination of the basis elements. This procedure is done for the wavefunctions representing each particle in such a way that the energy is minimized, populating the different energy levels so the Pauli Exclusion Principle is also satisfied. The quality of the result will be highly dependent on the quality of the basis set and the principle only states that the "best" solution in that subspace may be found. The second way the variational principle is applied is aimed at the derivation of a new Hamiltonian. In the derivation of the Hartree-Fock equations, the solution of the Schrödinger equation is assumed to have the format of a Slater determinant (see Equation 2.9), which is the simplest form that satisfies the antisymmetric requirement for the wave functions. Since a solution of this form does not satisfy the Schrödinger equation, it is assumed that the closest wave function can be found by applying the variational principle into wave functions of this form. As a result of this procedure a modified Hamiltonian is derived and this result is known as the Hartree-Fock equations. Finally, in DFT it can be proven that the electron density satisfies the variational principle. In this case, the variational principle is applied to an

.

expresion of the energy as a functional of the density to obtain equations that gives the wavefunctions of fictitious non-interacting particles. In this case, the orbital interpretation of the square of the wavefunctions is still commonly used, but not without some controversy. In the DFT framework provided that we have the exact exchange correlational functional, which is unknown (see Section 2.2.3) exact electron densities an energies and other derived observables can be calculated. In the textbook by Thijssen[7] there is an interesting derivation of the Schrödinger equation that performs a variational calculation of the energy as a functional of the wave function. On the other hand, Burke's book[8] has a good interpretation and comparison of the significance of Hartree-Fock and the Kohn Shan (DFT) orbitals.

2.2.3. Density Functional Theory (DFT)

The primary concept and the main difference for other methods such as Hartree-Fock is that DFT makes the electron density the central quantity from which all observables are derived, and abandons attempting to construct an estimate of the all-electron wave function. The first predecessor to modern DFT is the work by Thomas and Fermi in 1927, three years before the Hartree Fock method was published. This did not receive much attention at the time, but in the 1960's Kohn and coworkers published two papers[9, 10] that constitute the basis for modern DFT. Since then, DFT has become one of the more studied approaches to solving the many electron problem in both solid state physics and quantum chemistry applications. As in Hartree-Fock theory, we end up with a set of independent one-electron equations that can be solved self-consistently.

To study the strengths and weaknesses of DFT theory, its, we first briefly analyze the Hartree and Hartree-Fock methods. As we mentioned earlier, Equation 2.5 is too difficult to solve numerically for even a few electrons. Its main difficulty lies behind the electron-electron coulombic interactions that tie all the variables together. The Hartree method is one of the first approximations that tried to deal with these complexities; it ignores the antisymmetric characteristic of the all electron wave functions and proposes that the solution to Equation 2.5 can be written in the following form:

.

$$\Psi(x_1,'...,x_N) = \sum_{l=1}^{N} \psi(x_l) \tag{2.7}$$

Applying the variational principle to the former equation because it does not satisfy Equation 2.5, we seek for the closest wavefunction to the one from Equation 2.5 in a variational sense. The result is the Hartree equation:

$$\left[-\frac{1}{2}\nabla^2 - \sum_n \frac{Z_n}{|r - R_n|}\right]\psi_k(x) + \sum_{l=1}^{N} \int |\psi_l(x')|^2 \cdot \frac{1}{|r - r'|} \cdot \psi_k(x)dx' = E' \cdot \psi_k(x) \tag{2.8}$$

The term that contains $1/|r_i - r_j|$ was eliminated by assuming that one electron is moving in the average field originating from all the other electrons in the system. As a consequence, and by not requiring antisymmetric characteristics, the electrons are uncorrelated, i.e, the probability of finding one electron in a point on space is independent of the location of all the other electrons. This clearly violates Pauli Exclusion Principle, and the fact that electrons will try to avoid each other as a result of Coulombic interactions.

Unfortunately, the assumptions made in the derivation of this equation are too restrictive and the results that can be obtained from solving Equation 2.7 are not sufficiently good enough to realistically model most chemical systems. So, simply ignoring the antisymmetric character of the wavefunction leads to unsatisfactory results. The next level in complexity is one that can model the antisymmetric character of the wave function in the most simple way by assuming that the all electron wave function can be written as a single determinant of one electron waves, this is the so called Slater determinant and it can be written as:

$$\Psi = \frac{1}{\sqrt{N!}} \begin{vmatrix} \chi_i(X_1) & \chi_j(X_1) & \cdots & \cdots & \chi_k(X_1) \\ \chi_i(X_2) & \chi_j(X_2) & \cdots & \cdots & \chi_k(X_2) \\ \cdots & \cdots & \cdots & \cdots & \cdots \\ \cdots & \cdots & \cdots & \cdots & \cdots \\ \chi_i(X_N) & \chi_j(X_N) & \cdots & \cdots & \chi_k(X_N) \end{vmatrix} \tag{2.9}$$

Applying the variational principle to the Slater determinant (Equation 2.6) leads, after a lengthy derivation, in the books by Szabo[11] or Thijssen[7] to the Hartree-Fock equations:

$$\left[-\frac{1}{2}\nabla^2 - \sum_n \frac{Z_n}{|r-R_n|}\right]\psi_k(x) + \sum_{l=1}^{N}\int |\psi_l(x')|^2 \cdot \frac{1}{|r-r'|}\cdot \psi_k(x)dx' + $$

$$+\sum_{l=1}^{N}\int \psi_l^{*}(x')\cdot\frac{1}{|r-r'|}\cdot\psi_k(x')\cdot\psi_l(x)dx' = E'\cdot\psi_k(x) \tag{2.10}$$

The last term on the left hand side is called the exchange functional, distinguishes Hartree-Fock from Hartree equations and it is a purely quantum mechanical effect that mathematically describes Pauli Exclusion Principle. Hartree-Fock equations have been widely used in computational chemistry; they give in general good molecular geometries and satisfactory energies. With the help of Koopman’s theorem, excitation energies can be calculated and attempts to improve the method, for example by perturbation theory have also been conducted. The last term, the exchange-correlation functional, makes it computationally demanding but it has been and still is widely used.

Thomas-Fermi theory is the predecessor to modern density functional theory. As already stated its development took placed a few years before publication of the Hartree Fock method. However, as in case of the Hartree method, it is not accurate enough for chemical applications. The main difference between Thomas-Fermi theory and modern DFT theory is the way in which the kinetic energy is represented. The idea of obtaining the kinetic energy directly from the electronic density is abandoned by DFT and now the

.

real density of the system is expressed as the one resulting from the wave functions of fictitious non interacting particles:

$$\rho(r) = \sum_{l=1}^{N} |\psi_l(r)|^2 \tag{2.11}$$

From these wave functions, the exact kinetic energy for the fictitious non interacting particles can be calculated accurately can be obtained in the usual way as:

$$T[\rho] = \sum_l \frac{\hbar^2}{2m}(\nabla\psi_l)^2 \tag{2.12}$$

The energy as functional of the electron density can be written as:

$$E[\rho] = V_{ext}[\rho] + T[\rho] + V_H[\rho] + E_{xc}[\rho] \tag{2.13}$$

where:

V_{ext} is the contribution to the energy functional due to the external field, i.e. the positions.

V_H is the potential energy due to electrons Coulombic interactions.

T is the kinetic energy of the fictitious non-interacting electrons

E_{xc} are the contributions to the total energy that are not included in the other terms.

The final self-consistent equation can be derived by applying the variational principle to Equation 2.13 and is given by:

$$-\frac{\hbar^2}{2m}\nabla^2\psi_l + \left\{ U(r) + \int \frac{e^2 n(r)}{|r - r'|} dr' + \frac{\partial\varepsilon_{xc}(n)}{\partial n} \right\} \psi_l(r) = \varepsilon\psi_l(r) \tag{2.14}$$

The term $\frac{\partial\varepsilon_{xc}(n)}{\partial n}$ is the exchange-correlation functional, whose exact form is unknown. It maps the real interacting particle problem into the fictitious non-interacting one. Depending on the form of the exchange-correlation functional we can say that the

.

computational demands for solving Equation 2.14 are in general lower than the one associated with the solution of Hartree-Fock equation (Equation 2.10). Burke's book[8] constitutes a valuable source for DFT principles while solid state textbooks[12, 13] are required if one wants to study the applications of DFT equations in periodic systems.

Regarding the different possible functional selections, unfortunately the correct choice among available exchange-correlation functionals is a question of testing and experience. The reader is referred to the articles of Perdew and Burke[14] and Perdew et al.[15] and the books by Koch[16] and Martin [17] for addditional information in this topic.

As an example of the behavior of density functionals, we can mention that a well-known characteristic of LDA, i.e. local density approximation functionals, is their tendency to overbind. This is due to LDA functionals favoring a more homogeneous distribution of the electron density. Despite of that, when applied in calculations that depend on changes of energies *on the same system* the error tends to cancel out and that is why good geometries and frequencies can be predicted out of relatively bad energies from LDA calculations; this characteristic is shared with Hartree-Fock calculations.

2.2.4. Hilbert Spaces and Schrödinger's Equation

In Equation 2.1 we implicitly introduced the bracket notation. Implicitly we were moving out of the format of the Schrödinger equation as a complex partial differential equation, and going towards a more useful algebraic view. In this, a solution of the Schrödinger equation is an element of a vector space. Physical restrictions that are required to be fulfilled by acceptable solutions to Schrödinger further refine this concept. Thus, a solution of the Schrödinger equation is an element of a vector space that has a defined norm; this is called a Hilbert space. Wave functions should be squarely integrable due to the fact that there should be a finite probability of finding a given electron in a range spanning the entire space. The main advantage of this view, associated to the wave functions, is that provided we find a basis for the vector space any other vector and thus the solutions can be written as a linear combination of the vectors in the basis. The dimension of functional spaces (more specifically the ones that satisfy the requirements outlined above) is infinite and thus in theory infinite number of vectors is required to form the basis. Thus, any finite basis set will be a subspace, and therefore any solution found will be a projection of the real (but unknown) solution into this subspace.

An equation of the form:

$$\hat{A} \cdot \vec{x} = \lambda \cdot \vec{x} \tag{2.15}$$

where $\hat{A}$ is a linear operator (in any vector space as R^3, R^2, squarely integrating functions etc), $\vec{x}$ is an element of the vector space and λ is a scalar. This constitutes an eigenvalue-eigenvector problem which can be taken into a matrix form after a suitable basis for the given vector space is found. The Schrödinger equation is also an eigenvalue-eigenvector problem, the operator $\hat{H}$ is a linear operator acting on a function $|\Psi\rangle$ to give a scalar E multiplied by the function $|\Psi\rangle$. The realization that wavefunctions can be seen as eigenvectors in an eigenvector-eigenvalue problem provides powerful mathematical tools that allows as to map a complex differential equation into a simpler eigenvalue-eigenvector that can be solved with numerical diagonalization techniques (see for example Appendix M in Martin's book[17] and references therein) on condition that we find a suitable basis set. A very complete review of the mathematical tools associated with density functional theory can be found, for example, in the works by Burke [8] and Carbó-Dorca[18]

2.2.5. DFT on Periodic Systems

To use DFT to represent and handle extended systems, as in the case of solids or surfaces where the total number of atoms is on the order of Avogadro's number, some approximations must be made. The simplest approach, consistent in the study of a small portion of the system and extrapolating the results to the extended one does not apply because of the high ratio of surface to bulk atoms in this type of models. It is therefore

.

better to consider a small single cell which is assumed to be repeated an infinite number of times in one or more spatial directions. This condition of periodicity of the unit cell implies that the external potential, i.e. the potential term in the Schrödinger equation Hamiltonian associated with the nuclei positions, has the same periodicity as unit cell. Mathematically:

$$V(r) = V(r + R) \tag{2.16}$$

where R is the unit cell length.

The question answered by Bloch is the conditions imposed by the periodicity of the potential on the wave functions. Bloch's condition is the mathematical expression of this requirement and states that the solution of the Schrödinger equation with a periodic potential is a periodic function *u* of the crystal periodicity modulated by a plane wave. Mathematically:

$$\psi_{nk}(r) = e^{ik \cdot r} \cdot u_{nk}(r) \tag{2.17}$$

The vector k in Equation 2.16 is associated with the state of the electron in the extended system. This is analogous to the principle quantum numbers that define the state of an electron in an isolated atom. Indeed, k together with the band index n are the quantum numbers for the electrons in the solid. As will be discussed later there are essentially countless possible states in an extended system. The periodic function $u_{nk}(r)$ that has the same periodicity of the crystal is often written as a plane wave expansion. Basically, the quantum numbers result from the extreme case of a homogeneous electron gas in a periodic potential where V=0. In this case, the solution to the Schrödinger equation will simply be:

.

$$\psi_{nk}(r) = \frac{1}{\sqrt{V}} e^{ik \cdot r} \qquad (2.18)$$

and the possible states are given by $k=2\pi/L(k_1,k_2,k_3)$ such that k_1, k_2, k_3 are entire positive numbers. This notation can be further abbreviated by noting that the possible values of k form a Bravais lattice so the knowledge of the states in the unit cell of this lattice will suffice to describe the electronic states of the entire lattice. This phenomenon is the origin of the bands shown in Figure 2.2. In Figure 2.1 the direct space unit cell for solid platinum is shown, and to the right we can see the associated unit cell representing the set of possible values for (k_1,k_2,k_3). The surfaces inside the unit cell shows a special set of k values with energy equal to the Fermi energy, or highest energy with occupancies different from zero. The right and left side of Figure 2.1 are drawn out of scale, since the unit cell size in reciprocal space is related to the one in direct space by $2\pi/a$, where a is the lattice constant in direct space. In Figure 2.1, we can see that for a given k many different energy values are possible, each one on a different band. In general the number of bands will increase as we increase the size of the unit cells, with more nuclei and thus more electrons in the unit cell. In any case if the set up is correct the descriptions under different unit cell sizes will be equivalent. We note in Figure 2.2 the band gap on silicon, an insulator, that is absent in platinum, a metal. The points L, Γ, X, and U are points with special properties (high symmetry points) appearing after making a path that travels inside and along the borders of Figure 2.1 (right).

.

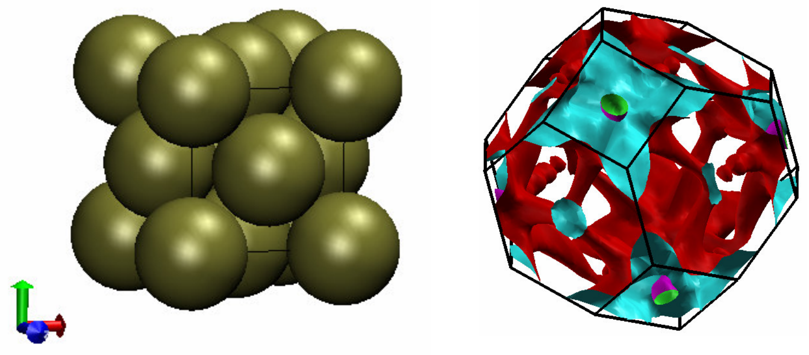

Fig. 2.1. Left: Pt crystal structure. Right: associated lattice structure in reciprocal space and its Fermi surface.

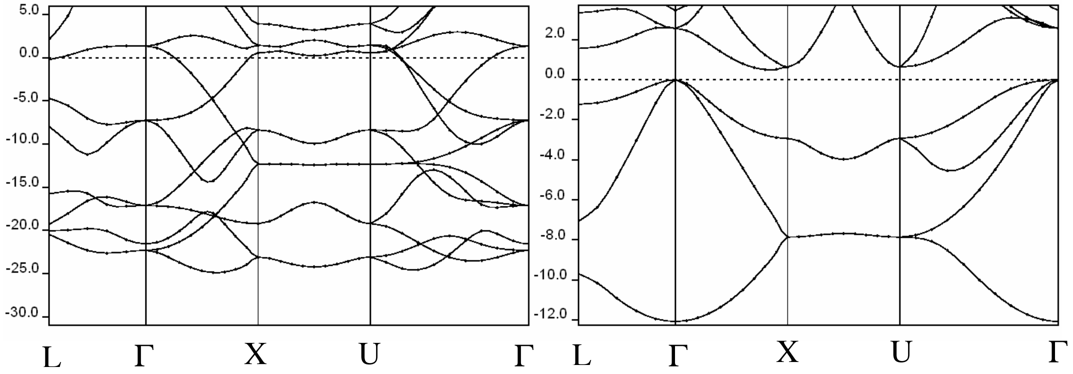

Fig. 2.2. Platinum (left) and Silicon (right) band structures.

We note that the band gap for Si is underestimated by the model, the experimental value is 1.12 eV, while the calculated value (estimated from Fig. 2.2) is about 0.3 eV. This is another well-known limitation of density functional theory. It is also worth noticing the wide range of values as we move in reciprocal space, given the different band gaps. We can imagine how a poor k-space sampling can affect the calculations, for example, for Pt on the left of Figure 2.2, we can see that it would be predicted to be an insulator if only the Γ point were to sample the reciprocal space for the cell size used to calculate the band structure (with two Pt atoms per unit cell). It is clear that good k-space sampling method is required to describe extended systems, especially the ones modeled by a few atoms in small unit cells. The method by Monkhorst and Pack[19] is one of the most commonly used algorithms for k-space sampling.

2.2.6. Plane Waves and the Pseudopotential Approach

In the previous section plane waves were introduced as the natural basis set for modeling periodic systems. There are advantages and disadvantages associated with this approach. Plane waves are orthogonal and easy to handle numerically through Fast Fourier transforms. Plane waves are completely delocalized, i.e. all regions of space are equally covered (i.e., no need of polarization functions etc.), there are no superposition errors and no Pulay forces. The completeness of the plane wave expansion is easily defined by the number of plane waves through the plane wave cut off. There are also well known limitations associated with this approach. Since this basis set is completely delocalized there is no distinction between regions with high and low electronic density, making it less efficient in handling systems with large vacuum regions. Planes waves are also inefficient at describing core electrons where an unacceptable large plane wave basis set would be required. To overcome this difficulty and yet work efficiently with plane waves we must introduce the concept of pseudopotentials. These are a modification of the Hamiltonian in the Schrödinger equation that replaces the core electrons by adding an extra potential term. As a result of this modification, the first eigenvalues and eigenvectors of the Schrödinger equation are now those corresponding to the valence electrons whose pseudo wavefunctions are also smoother and thus easier to describe with plane waves. Put simply, a pseudopotential is generated by fitting the pseudo-wave functions including some imposed requirements, to the real wave functions for the valence states. After the pseudo-waves are obtained, the Schrödinger equation is

.

inverted to obtain the parameters that define the pseudo-potential. In that way, the Schrödinger equation has been adapted to reproduce the valence wavefunctions and their energies.

The requirements of a pseudopotential depend on its type, for example, for norm conserving pseudopotentials Hamann et al.[20] listed the following desirable properties:

a. All electron and pseudo-valence eigenvalues should agree for the chosen atomic reference configuration.
b. All electron and pseudo-valence wavefunctions should agree beyond a chosen radius r_c
c. The logarithmic derivatives of the all electron and pseudo-wavefunctions should agree at r_c
d. The integrated charge inside r_c for each pseudo and real wavefunction should agree (norm conservation requirement)
e. The logarithmic derivatives for the real and pseudo wavefunctions and their first energy derivatives should agree for $r > r_c$

As mentioned above, the requirements depend on the type of pseudopotential. For example, requirement d is not enforced in the so called Vanderbilt ultra soft pseudopotentials[21], in which the norm-conserving rule is relaxed. In such cases, it is possible to work with a much smaller plane wave basis sets at the expense using compensation charges.

Since the core electrons can be considered as being chemically inert, pseudopotentials may perform well in chemical environments that leads to electron configurations different from those used during the fitting process. The study and verification of the pseudopotential behavior under different chemical environments during its generation are known as transferability studies. Usually these studies can be run in two ways. First after generating the pseudopotential a few more runs are made with different occupancies from those of the ground state in order to mimic different chemical environments. The results of such runs are shown for the Pt pseudopotential in

.

Table 2.1. The second approach is to run the pseudopotential in known chemical environments and compare geometries and energies with known data, preferably obtained via other verifiable calculations or experiment. Figure 2.3 shows the pseudo and valence wavefunctions for Pt. We note that the d channel match is after the maxima in the wavefunction and the area under the curves are not the same for pseudo and real waves. This is what makes that channel "ultrasoft", i.e. non norm-conserving.

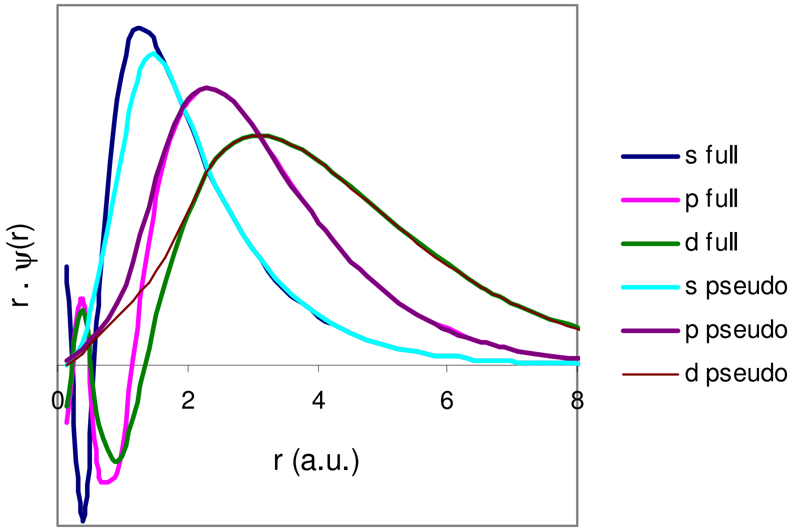

Fig. 2.3. All electron and pseudo radial wave functions for a Pt pseudopotential generated using Vanderbilt's method and code.

.

Table 2.1.

Transferability tests for the Pt pseudo, where the 5d9, 6s1, 6p0 was the reference state used to generate the pseudopotential.

States	E all electron (Ry)	E pseudo (Ry)	diff
5d9	–0.451391	–0.451392	0.000001
6s1	–0.415925	–0.415927	0.000002
6p0	–0.061745	–0.061744	–0.000001
5d10	–0.327912	–0.326810	–0.001102
6s0	–0.359367	–0.363004	0.003637
6p0	–0.040779	–0.042323	0.001544
5d9	–0.491903	–0.491707	–0.000196
6s0.75	–0.446896	–0.447165	0.000269
6p0	–0.085348	–0.085417	0.000069
5d9	–1.051339	–1.050064	–0.001275
6s0	–0.946619	–0.949126	0.002507
6p0	–0.489252	–0.491004	0.001752

.

3. SURFACE REACTIONS

> The fundamental laws necessary for the mathematical treatment of a large part of physics and the whole of chemistry are thus completely known, and the difficulty lies only in the fact that application of these laws leads to equations that are too complex to be solved.
>
> \- Paul Dirac

3.1. Introduction

Many issues and improvements are being studied on fuel cells and hydrogen production and storage with the goal of reaching an economically viable alternative to hydrocarbon fuels for producing energy. Fuel cell components being actively researched include hydrogen storage and generation, better carbon monoxide resistant anode catalysts, a more efficient and less expensive proton transport membrane, and better cathode catalysts. In this review section we will focus exclusively on the last problem, the search for more efficient and less expensive cathode catalysts with improved understanding of the reaction mechanisms and characterization of their intermediates on catalytic surfaces. This review is divided into two sections; the first is a summary of the conclusions reached over the years by experimentalists concerning these reactions in different catalysts. The second part summarizes the effort resulting from computer models to provide arguments for explaining experimental observations.

3.2. Experimental Works

3.2.1. Pt and Pt Alloys as Catalysts for Oxygen Electroreduction

For many years platinum has been the catalyst of choice for the oxygen electroreduction reaction (OERR). Platinum has many advantages over some of the other alternatives, it is the most catalytically active among pure elements and it is relatively stable in the highly corrosive environment of an acid electrolyte fuel cell. However, the cathode is still the main source of power loss in acid fuel cells due to the poor kinetics of

.

oxygen reduction reaction. In contrast the hydrogen anode proceeds nearly at its maximum theoretical rate: in fact, under ordinary conditions the hydrogen oxidation rate is nearly 10^7 times faster than the oxygen reduction rate[22]. High platinum costs and low availability will result in high overall fuel cell costs. Interest in Pt alloys as possible pure-Pt replacement candidates is not new, in the past few years other alternatives have been also evaluated, among which are Pd alloys, metalloporphyrins,[23] and others. In this part of the review section, we will focus on experimental efforts to identify improved catalysts for the OERR, with emphasis on the systems associated with this dissertation, that is, Pt and Pd alloys in acidic media and in the experimental determination of the reaction mechanism.

Oxygen electroreduction in acidic media may occur through either one or a combination of two different pathways. The *direct* pathway that involves O–O bond breaking before a second proton is attached to the molecule, while the *series* pathway generates hydrogen peroxide as an intermediate. Schematically, Wroblowa represented these two pathways as[24, 25]:

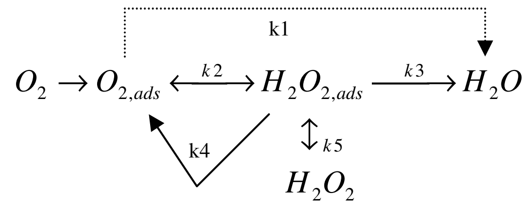

(3.1)

The k_i values in 3.1 are the kinetic rate constants associated with each process. The process associated with k_1 is the direct mechanism, whereas the series mechanism involves the formation of adsorbed H_2O_2 (rate constants k_2 and k_3)

In earlier work, Damjonovic and Brusic[26] experimentally studied the kinetics of O_2 reduction in an oxide-free Pt electrode. In acid solution, the authors eliminated three possible mechanisms because they failed to explain the pH and O_2 partial pressure dependences. They also argued that the first and last reaction steps might be:

$$O_2 + H^+ + e^- \xrightarrow{Pt} O_2H \quad \text{(first step)} \tag{3.2}$$

$$OH + H^+ + e^- \xrightarrow{Pt} H_2O \quad \text{(last step)} \tag{3.3}$$

They also stated that the first step was rate-determining and that the detailed mechanism after the rate-determining step (RDS) was unknown. Based on the assumption of reaction (3.2) being rate determinant they derived the following rate equation:

$$i = k \cdot p_{o_2} \cdot a_{H^+}^{3/2} \cdot e^{-F \cdot V / R \cdot T} \tag{3.4}$$

The authors also considered the possibility that above first step was not the RDS; in such a case, they hypothesized that O_2 first adsorbs weakly on the metal surface in the following equilibrium:

$$O_2 + S \xleftrightarrow[S=Pt]{} S \cdots\cdots O_2 \tag{3.5}$$

They then speculated that the RDS might be in one of the following two steps

$$S \cdots\cdots O_2 + H^+ + e^- \xrightarrow{Pt} S \cdot OH + SO \tag{3.6}$$

$$S \cdots\cdots O_2 + H^+ + e^- \xrightarrow{Pt} S \cdot O_2H \tag{3.7}$$

where S is a surface site and on the which O_2 appears is weakly bounded to the surface.

In a 1970 review, Appleby[27] analyzed the oxygen reduction reaction in acid media, concluding that the initial electron transfer to an adsorbed oxygen molecule is rate determining on phase-oxide-free surface of Group Ib and Group VIII metal alloys. He considered that the location of the RDS was:

$$S \cdot O_2 + H^+ + e^- \xrightarrow{Pt} S \cdot O_2H \tag{3.8}$$

.

which was supported by pH dependence studies of the OERR. The author found volcano-type plots when plotting current density (an indicator of the catalyst activity) against d band vacancies, heat of sublimation and oxygen adsorption energies for different pure transition metals (Ag, Au, Rh Pd, Pt, Ir, Ru and Os) and some Pt alloys with Ru alloys, with Pt in all cases at the top of these plots. He estimated that preexponential factors for the Pt surface closer to the ones found in the much faster hydrogen reaction. The main kinetic problem was in the activation energies, which were much higher than in the hydrogen case. In addition, attempts directed at lowering this activation energy resulted in compensation effects in the preexponential factor, painting a grim picture regarding the prospects of catalytic improvement following this type of strategy.

In contrast, Yeager[28] proposed a direct mechanism for the OERR in acid media solutions on oxide-free Pt surfaces, i.e. under similar conditions to the work of Damjonovic and Brusic[26]. This can be summarized as follows:

$$\begin{array}{ccccc} B' \quad O & & B' \;\; O & & B'-O \\ A + \; \| & \xrightarrow{Pt} & A \, \langle \; | & \xrightarrow{Pt} & A \\ B \quad O & & B \;\; O & & B-O \end{array} \tag{3.9}$$

$$B'{-}O + H_3O^+ + e^- \xrightarrow{Pt} B'{-}OH \tag{3.10}$$

$$B - O + H_3O^+ + e^- \xrightarrow{Pt} B - OH \tag{3.11}$$

$$B'{-}OH + H_3O^+ + e^- \xrightarrow{Pt} B' + H_2O \tag{3.12}$$

$$B - OH + H_3O^+ + e^- \xrightarrow{Pt} B + H_2O \tag{3.13}$$

where B and B′ are the opposite hollow sites to the top site A.

Based on experiments in deuterated phosphoric acid Yeager claimed that there is evidence that the proton is not involved in the RDS, which is one of the reactions involving the adsorption of oxygen. At more positive potentials where an anodic layer might be present; the RDS may either the adsorption or dissociation of oxygen.

Mukarjee and Srinivasan[29] found a 2 to 3 fold increase in catalytic activity on carbon-supported Pt_3Cr, Pt_3Ni and Pt_3Co alloys. They characterized the lattice structures of the nanoparticles and found lattice contractions in all alloys; the enhancement in catalytic activity was in part attributed to this. The authors also suggested a possible mechanism change on the alloys, since they found lower activation energies and different reaction orders compared with experiments on carbon-supported Pt electrocatalysts. In a later work Mukarjee et al.[30] attempted to further explain the sources of observed catalytic enhancements by X-ray Absorption Near Edge Structure (XANES) and Extended X-Ray Absorption Fine Structure (EXAFS) studies on five Pt alloys (Pt_3M with M equal to Cr, Mn, Fe, Co or Ni). This study confirmed the catalytic enhancement upon alloying, and established the following succession of increasing rate: PtCr/C > PtFe/C > PtMn/C > PtCo/C > PtNi/C > Pt. The enhancement was attributed to a combination of electronic (d band vacancies change) and geometrical changes (lattice contraction upon alloying). These in turn changed the affinities of the catalysts towards OH adsorption. Plots of these parameters against catalytic activity showed volcano-type plots with the PtCr alloy located in the top.

Grgur et al.[31] investigated the OERR kinetics on various crystallographic faces and attributed the different activities found to differences in adsorption of hydroxyl, halides and bisulfates on the different faces. They claimed that the result of experiments using rotating ring disk measurements provided evidence that the series mechanism (via an HO_2 intermediate) is active and that the first electron transfer is the RDS.

Toda et al.[32] investigated the catalytic activity of Pt alloys with Fe, Ni and Co at different compositions. They found enhanced activity in all studied alloys when compared with pure Pt being the optimum composition different in each bimetallic surface: 30% Ni (10 times more active than pure Pt), 40% Co (15 times more active than pure Pt) and 50% Fe (20 times more active than pure Pt). They also found Pt skin formation in all the surfaces studied that is, the first few layers on each surface are pure

.

Pt. These authors attributed the catalytic enhancements to a different electronic structure in the d band for the Pt atoms located at the surface compared to those found on pure Pt surfaces. They discarded surface roughening and different ratio of crystallographic size as the source of the difference in activities between catalysts.

Paulus et al.[33] pointed to inconsistencies in the literature regarding catalytic enhancement due to alloying. They stated that differences in particle size and shape in supported catalysts and roughening and faceting in smooth electrodes contributed to these discrepancies. This made the comparison between alloys difficult, and that careful catalyst preparation was necessary to obtain comparable samples. In a comparable set of bimetallic catalysts, these authors observed catalytic enhancements of a factor of 1.5 per unit electrode area in case the of bulk electrodes (in both cases Pt-Co and Pt-Ni alloys), 1.5 to 2 for supported 75% Pt catalysts (again both Pt-Co and Pt-Ni alloys) and a factor of 2 to 3 for the 50% PtCo catalyst. They proposed that the same reaction mechanism occurs on all catalysts studied, a series mechanism, and that the enhancement is due to a change in the preexponential factor in the rate equations. This factor is a function of the hydroxyl coverage in the surfaces. They also stated that the higher enhancements reported by Toda et al. might be due to an abnormally low pure Pt activity they reported, which was used throughout their calculation as a reference to estimate the enhancements.

3.2.2. Pd and Pd Alloys as Catalysts for Oxygen Electroreduction

Despite being near the top of volcano plots representing catalytic activity[22], early reports on the use of pure Pd use as electrocatalyst shows that this metal exhibits a differentiating behavior when compared with pure Pt due to its higher reactivity. Burke and Casey[34] described the Pd electrode in acidic media as prone to dissolution and with tendency to develop a growth of a OH layer reduces performance of the catalyst over time. Fernandez et al.[35] reported catalytic activity comparable to that found for pure Pt in two Pd alloy catalysts: a ternary alloy Pd-Co-Au (70:20:10 atom %) and a binary Pd-Ti (50:50 atom %). Initial performances were comparable to those found in pure Pt,

.

with the ternary alloy being slightly better. However, while the bimetallic catalyst showed good stability, the ternary alloy showed performance degradation with time. The authors speculated that this was possibly due to Co leaching to the fuel cell environment. This study also reported much lower methanol oxidation currents on such electrodes. This is a desirable effect in direct methanol fuel cells, since it signals an increased tolerance to methanol crossover. In later work, Raghuveer at al.[36] analyzed a different ternary alloy Pd-Co-Mo (70:20:10 atom %) and claimed a slightly better performance than Pt without the catalyst degradation found in the Pd-Co-Au.

Lee and collaborators[37] studied Pd bimetallic alloys and their activity towards O_2 reduction on direct methanol fuel cells. They established the following trend in catalytic activity when methanol is present Pd-Ni > Pd-Co > Pd-Cr > Pd. In all cases, the optimum mixture for the Pd-M alloys was 60:40 % atom.

3.2.3. Summary and Conclusions

The OERR in acidic media seems to proceed according to the general scheme proposed by Wroblowa with either the 4 e^- series mechanism or a combination of the series and direct mechanisms. The exact details of the mechanism for OERR remain unclear after many years of study. Most authors identify the first proton and electron transfer as the possible rate determining step.

There is experimental evidence that the OERR proceeds faster in Pt alloys (with Co, Fe or Ni) than on pure Pt, but the source of this improvement is still somewhat unclear, with a change in the preexponential factor (due to different OH coverages) as one of the possibilities.

Experiments on Pd surfaces show that the slightly higher reactivity of this surface is enough to create some problems in fuel cell operation by generating oxide layers over the surface and subsequent deterioration on catalytic activity. On the other hand, some research in Pd alloys has shown promising results with activity comparable to Pt and good activity conservation and lower methanol oxidation rates.

.

3.3. Theoretical Research

3.3.1. Introduction

The review section for the application of theoretical tools to the understanding of the oxygen electroreduction reaction is organized in a rather different way to that of the experimental review. This is due to the nature of the tools used which makes easier for the observer to focus on details with perfect control over the conditions, for example, whether or not allow surfaces to relax, ignoring the solvent or incorporating it explicitly or via mean field approximation, using different levels of theory, etc. In part, these advantages are of course related with the main difficulties associated with the employment of Ab Initio techniques to the study of surface reactions. The broader picture becomes increasingly difficult as the associated computational costs increase as higher levels of theory or time and space scales are used. In this section, we review the main contributions to the interpretation and characterization of chemical bond in surfaces, the adsorption of individual adsorbates in small clusters or extended surfaces, and we finish with more detailed calculations that for example include the addition of electric fields, solvent effects and the study of complete reaction profiles.

3.3.2. Characterization of Transition Metal Surfaces

As was discussed in the introductory section, the handling of large numbers of electrons associated with extended ordered systems such as surfaces or solids via modeling with periodic boundary conditions gives rise to plots of electronic states versus energy called band structures. Hoffmann[38, 39] published one of the first works that linked concepts originated in the treatment of completely delocalized electronic states with the more localized bonding concept that came from hybridization of atomic orbitals. In these works, Hoffmann reviewed several techniques used in the study of surface reactivity and bridges the concept of band structure, frequently used in physics,

.

with the chemist more familiar concept of molecular orbitals through density of states. He described the interaction of carbon monoxide with a transition metal,[39] and analyzed bonding in terms of localized density of states. Adsorbate-surface were described based on the metal sp and d states. This concept was further refined in an important contribution by Hammer and Norskov[40], who observed that the location of the entire d-band with respect to the Fermi level as measured by its first moment of inertia, also called the d-band center, is the key variable in establishing reactivity trends on transition metal surfaces. The success of the d-band model has been verified and repeatedly applied since its publication.[41] In Section 5, we verify this model for various Pt and Pd alloy surfaces. The importance of the d-band as a catalyst design parameter has been also stressed, and new work has applied this concept to catalyst design, (see for example[42, 43]). Recently, Greeley and Norskov[44] have applied the model to estimate adsorption energies on transition metal alloys.

3.3.3. Ab Initio Studies of Oxygen Electroreduction Intermediates

Molecular and atomic oxygen adsorbed on Pt are perhaps the most intensively studied intermediates of oxygen electroreduction processes. Feibelman and collaborators[45] estimated adsorption energies for oxygen atoms on stepped Pt(111) surfaces. These authors described preferred adsorption sites based on energy considerations, ond observed that Pt coordination number was an important factor selecting preferred adsorption sites. They found that *fcc* sites are preferred over *hcp* sites by 0.4 eV (extending the concept of *fcc* and *hcp* to sites near the edges of stepped surfaces). They also found that an oxygen adatom gains energy in proportion to the number of nearest neighbors that are step-edge atoms (0.25 eV for one, 0.4 eV for two and 0.6 eV for three nearest edge-atoms). These arguments explained observed features in scanning tunneling micrographs obtained on these systems. In a later work, Feibelman[46] explained the high energy difference between *fcc* and *hcp* adsorption sites as based not on a stronger Pt –O bond because of a reduced weakening of Pt-Pt bonds

.

between the first and second layer Pt atoms lying below the adatom. According to this author this weakening is caused by electrostatic repulsion of the negatively charged O adatom so that the Pt d-electrons form antibonding states between the Pt atoms and their nearest neighbors. On the *hcp* sites this bond weakening is more pronounced because the number of affected atoms is higher. Similarly, Bogicevic, Stromquist and Lundqvist[47] corroborated the large difference in adsorption values obtained by Feibelman and estimated the diffusion barrier from an fcc to an hcp site to be 0.58 eV and 0.68 eV using generalized gradient approximation (GGA) and local density approximation (LDA) functionals. This discrepancies in the calculation depending on functional was attributed to a better agreement between LDA and GGA functionals in adsorption sites with higher electron density, as in the case of hollow sites, while this agreement becomes less for intermediate bridge sites.

Jacob et al.[48] calculated adsorption energies and preferred adsorption sites for atomic oxygen at different sites in Pt clusters of different sizes. They concluded that a three layer 28 atom Pt cluster gives a good representation of the Pt(111) and its possible adsorption sites. They found that the fcc hollow site is preferred, with an adsorption energy of 3.28 eV followed by hcp hollow site with 2.95 eV and top site with 2.02 eV.

In series of papers, Eichler et al.[49, 50] and Grob et al.[51] studied oxygen dissociation pathways using DFT plane wave calculations together with the PW91 exchange correlation functional on a Pt (111) surface. In the pathways they found several local minima identified as molecular precursors of the dissociated state. They identified two molecular precursors: the first, a superoxo-like O_2^-, adsorbed in a t-b-t position with an adsorption energy equal to –0.72 eV per molecule and O–O bond length of about 1.39 Å, the second precursor, a peroxo-like O_2^{2-}, adsorbed in t-fcc(hcp)-b with an adsorption energy equal to –0.68 eV and O–O bond length of 1.43 Å. They identified these precursors as the ones observed experimentally, with measured bond distances of 1.37 Å for the first and 1.4 Å for the second, and measured adsorption energies –0.4 eV and –0.5 eV. The same system was studied by Bocquet et al.[52] who confirmed the presence of both precursors, simulated STM images and reported adsorption energies of –0.64 eV

.

for O_2 in bridge site (–0.53 eV on the unrelaxed surface) and –0.65 eV for O_2 in fcc hollow site (–0.47 eV in the unrelaxed surface). They confirmed that both precursors are nearly degenerate. Xu, Ruban and Mavrikakis[53] revisited O_2 adsorption and dissociation problem from a slightly different perspective by studying on Pt(111), a skin Pt(111), a 2% compressed Pt(111) and a Pt_3Co(111) and Pt_3Fe (111). They studied both the case where Co and Fe are present in the surface and the Pt skin case. They found that the ordering for binding energies follows the trend: skin Pt(111) < compressed Pt(111) < Pt(111) < Pt_3Co(111) ~ Pt_3Fe (111). These authors also verified a linear relation when adsorption energies are plotted against the d-band centers, verifying Hammer and Norskov's predictions[40]. The calculated activation energies required for O_2 dissociation using the nudged elastic band method showed that for the less reactive surfaces, i.e., the Pt_3Co and the Pt_3Fe both with a Pt skin, higher activation energies equal to 0.93 eV and 0.89 eV per O_2 molecule respectively. They concluded that despite their lower reactivity these surfaces are more active towards O_2 reduction because they are less poisoned by adsorbed O and facilitate the activation of O and O-containing elements in the bond making steps of the oxygen electroreduction reaction.

Michaelides and Hu[54] studied hydroxyl adsorption at different coverages on Pt(111). According to their calculations, bridge and top sites are preferred and nearly degenerated (adsorption energy about 2.2 eV) at low and medium coverages (up to 1/3 monolayer, ML). The authors also studied OH diffusion barriers and estimated a barrier of 0.11 eV for OH diffusion concluding that OH has a high mobility which will favor OH island formation due to its tendency to become stabilized by coadsorbed hydroxyl groups due to hydrogen bond formation. At higher coverages, up to 1 ML, they found enhancements in adsorption energies (from 2.2 eV per hydroxyl group to 2.53 eV at coverages over 1/2 ML) due to hydrogen bonding and preference for adsorption on top. Roques and Anderson[55] calculated adsorption energies for OH and H_2O at different OH coverages and analyzed O_2 adsorption on surfaces covered by 1/2 ML of OH on a Pt_3Cr (111) surface with Cr present on the surface. They concluded that is unlikely that

.

O_2 will be able to displace water under these conditions, speculating that there should be Pt islands available for O_2 adsorption possible due to Pt skin formation.

There is some controversy in the literature regarding the structure of saturated water layers on Pt(111). Ogasarawa et al.[56] based on experimental and theoretical observations described the first water layer as nearly flat (with an estimated width of 0.25 Å) with all the molecules binding to the surface or through H bonds and without dissociation. Febelman[57] analyzed reported results in similar cell sizes and concluded that larger cells ($p\sqrt{39}X\sqrt{39}R16.1^{\circ}$) are required to explain wetting. He argued that conclusions derived from those calculations showed that claims of water forming a highly ordered undissociated bilayer are questionable, and offered computational evidence of the presence of H_3O^+ and OH together with H_2O, on Pt(111).

The important role of OH adsorption on the catalyst surface has been identified; OH bonds strongly to the surface and has a tendency to accumulate slowing down the OERR kinetics by occupying active sites on the catalyst[33]. Held et al[58] studied the reaction of adsorbed oxygen and water finding as a result a mixed p(3 X 3) (3OH + $3H_2O$) phase on Pt(111) with oxygen atoms hydrogen bonded in a coplanar hexagonal arrangement near Pt top sites. Karlberg et al.[59] performed theoretical studies on the same reaction considering OH + H_2O and 2OH + H as the two possible products with two different surface representations, the $p3X3$ and the $\sqrt{3}X\sqrt{3}R30^{\circ}$. They found a slight difference of 19 meV per OH + H_2O in favor of the former, one and a larger difference (1.39 eV) for 2OH + H production in both cell sizes.

.

3.3.4. The Double Layer Electric Field and Cell Potential Effects

As pointed out by Anderson and Albu[60] one of the major difficulties in the advancement of the theoretical treatment of electrocatalysts has been the lack of an Ab Initio theory that includes the effect of cell potentials on the mechanisms, structures and activation energies of the electrode reactions. In early work using a single Pt-atom model to represent the surface, they built energy profiles with cell potential as a parameter while analyzing different possible reaction mechanisms. They analyzed both the O_2 reduction reaction and water oxidation. They concluded that the most favorable path on the O_2 reduction is the one where the O–O bond is broken just after the second protonation.

Panchenko et al.[61] investigated the interactions of OH, OOH. and H_2O_2 on different low indexes Pt surfaces: Pt (111), Pt(100) and Pt(110). They observed that hydrogen peroxide was unstable on all the different Pt facets, dissociating to give two adsorbed hydroxyls. They plotted energy profiles for each crystallographic facet, and concluded that reactivity was similar on (111) and (110), while it should be somewhat lower on the (100) face due to a minimum in the energy profile resulting from stronger OH adsorption. The effects of an electric field on the properties of adsorbed molecules were studied in a Pt_9 cluster. The electric field had intensities ranging from –0.01 a.u. to 0.01 a.u (with 0.0025 a.u. increments). The authors found dramatic changes in adsorption energies, geometries and vibrational frequencies due to the electric field. In an analysis on a Ag_{13} cluster with changes in electric fields as the same ranges as those explored above, Koper and van Santen[62] found less dramatic changes in the adsorption energies in H, O and OH. Recently, Norskov et al.[63, 64] examined the effects of the electric field of the electrochemical double layer on adsorption energies, and argued in favor of neglecting these contribution, which they estimated on the order of 0.015 eV, assuming a double layer thickness of 3 Å, and an electric field of about 0.3 V/Å. They also generated Gibbs free energy profiles for the oxygen reduction reaction through a combination of Ab Initio and thermodynamic data. Adsorbate energies and zero point

.

energies were calculated via Ab Initio techniques and formation entropies were obtained from thermodynamic tables.

3.3.5. Summary and Conclusions

The understanding of chemical properties of surfaces has seen a major advancement with the d-band model that underlines the position of the d-band center for a clean surface as the characteristic variable that will define its reactivity.

Oxygen adsorption has been the subject of extensive theoretical research. In general, despite divergences in the exact value, preferred adsorption sites and geometries and energies have been established in agreement with experimental observations. As an example, Table 3.1 shows a compendium of calculated adsorption energies for atomic oxygen. The divergences are mostly due to the sensitivity of Ab Initio methods to the calculation of energies and its dependence on functional, basis sets, and the type of model applied to the surface. Despite such success, some problems remain that are associated with the available functionals. For example, Hammer et al.[65] have published a report about functional performance describing adsorption energies mostly based on the Perdew-Burke-Ernzerhof (PBE) functional and its derivations for oxygen containing species. They found variability of up to 0.3 eV in adsorption energies for O_2 within the same functional family.

Contributions from different groups are beginning to add the effects of different variables to what has been an incomplete theoretical picture of the oxygen reduction reaction. The interaction of intermediates with the surfaces in the presence of an electric field is beginning to be taken into account, as is the presence of water and the cell potential. Recent discussions have shown that even the simplest systems, such as the case of pure water on Pt (111) are not free of controversy as greater computer power allows the theoretical scientist to work with larger cells, uncovering different structures of the water adlayer structure.

Table 3.1.

Comparison of adsorption energies for atomic oxygen in Pt(111) from different sources. Legends: NR = not reported, NE = not a true minimum, will go to a hollow site during relaxation.

Reference	Surface	Model	ΔE (eV) fcc hollow	ΔE (eV) hcp hollow	ΔE (eV) bridge	ΔE (eV) top
Ref. [48]	Pt_6 (111)	B3LYP Localized Basis Sets (Jaguar)	–2.68	–3.51	–2.63	NR
	$Pt_{8,4}$ (111)		–2.39	–1.86	–2.13	NR
	$Pt_{9,10,9}$ (111)		–3.28	–2.94	–2.72	NR
Ref. [61]	Pt (111)	APW-PW91 (VASP)	–4.08	–3.78	NR	NR
Ref. [45]	Pt (111)	LCAO-LDA (QUEST)	–5.28	–4.9	NR	NR
Ref. [53]	Pt(111)	PW-PW91-(DACAPO)	–3.88	–3.49	NE	–2.49
This Work	Pt (111)	PW-PBE (QE)	–3.73	–3.32	NE	–2.49

.

4. METHODOLOGY AND COMPUTATIONAL DETAILS

> If you want to know whether a duck is crossing the street,
> you look twice.
> - Harry Collins

4.1. Models, Parameter Selection and Scientific Software Used in This Work

This section starts the second and most important part of this dissertation. In the following sections we present results and conclusions obtained applying the techniques described in the introductory part. In this section the computational parameters adopted in our simulations are given and, unless otherwise specified, they are common to all calculations carried in Sections 6, 7 and 8.

DFT calculations of oxygen reduction reaction intermediates were performed on Pt, Pd, $Pd_{0.75}Co_{0.25}$, and $Pt_{0.75}Co_{0.25}$ using the plane wave framework. The unit cell is modeled as three layer (111) surface with 4 atoms per layer, as was previously used by others to successfully model adsorbate-surface interactions in similar systems[66-68]. In the bimetallic case, we studied two skin systems with the same Co distributions in Pt-based and Pd-based systems; in both cases the proportions of Co are 0% in the first layer, 50% in the second layer, and 25% in the third layer. Periodic boundary conditions are applied in the three spatial directions and 10 Å of vacuum space is left between periodic images in the direction perpendicular to the surface.

We adopted Vanderbilt ultrasoft pseudopotentials[21] to decrease the computational requirements associated with the description of inert core electrons, together with the PBE exchange correlation functional. All pseudopotentials are either obtained from Vanderbilt's library[69] or derived based on existing ones used as a reference. The Pd pseudopotential is based on a Rh pseudopotential available in the library and developed by Hansen, and designed with 2 s, 2 p, and 2 d nonlocal projectors and nonlinear core correction (*rcloc* = 2.2 a.u). The cut-off radii are set to *rc* = 2.64 a.u for the s and p channels, and *rc* = 1.55 a.u. for the d channel. In all cases transferability was verified: the results for Pd are shown in Table 4.1. This pseudopotential gives a cell constant expanded nearly 1% with respect to experimental results (a_0 = 3.926 Å). The plane wave cut off is set to 50 Ry and the first Brillouin zone is sampled with a Monkhorst Pack mesh with 7x7x1 k-points. To facilitate convergence, fractional occupancies are allowed applying the Mazzari-Vanderbilt cold smearing scheme.[70] The electronic temperature is set to 1000 K, i.e. adopting a smearing parameter of kT ~ 0.0325 eV.

Table 4.1

Transferability tests for the Pd pseudo, where the 4d10, 5s0, 5p0 was the reference state used to generate it.

State	E all electron (Ry)	E pseudo (Ry)	diff (Ry)
4d10	–0.297504	–0.297505	0.000001
5s0	–0.24414	–0.24414	0.000000
5p0	–0.023	–0.023	0.000000
4d9.75	–0.342907	–0.343394	0.000487
5s0.25	–0.262584	–0.262315	–0.000269
5p0	–0.032494	–0.032367	–0.000127
4d9	–0.564201	–0.568206	0.004005
5s0.5	–0.370635	–0.370208	–0.000427
5p0.5	–0.095426	–0.095157	–0.000269
4d9	–0.491517	–0.495178	0.003661
5s1	–0.320069	–0.319349	–0.00072
5p0	–0.058215	–0.057809	–0.000406

The geometries of the different species in this study are relaxed using the Broyden-Fletcher-Goldfarb-Shanno (BFGS)[71-74] method, ensuring that residual forces are below 10^{-3} Ry/au and with a change in total energy under 10^{-4} Ry between BFGS steps. The wave functions are converged in such a way that energy changes are under 10^{-6} Ry during self consistent iterations. In all cases, the calculations included spin polarization, and the non-zero magnetization states are taken into account in the Co alloys. All these convergence criteria were verified by running a few calculations with tighter

.

convergence parameters and checking geometries and energies against the data obtained with the above parameters.

In all cases the adsorption energy is calculated according to:

$$\Delta E = \frac{1}{n}\left(E_{S+nA} - (E_s - n \cdot E_A)\right) \tag{4.1}$$

where S is the clean surface, A the adsorbate and n the number of adsorbate molecules in the unit cell.

Changes in electron density originated by the surface-adsorbate interactions have been calculated according to Equation 4.2. They are graphically shown in Figure 4.1 for a weakly adsorbed hydrogen peroxide molecule which will provide us qualitative information regarding the electron flow due to adsorbate – surface interactions. In this example, this was performed for a hydrogen peroxide molecule weakly bonded to a $Pt_{0.75}Co_{0.25}$ surface. As we will see later, features observed in the metal atoms will appear again for different adsorbates. The areas in red in the figure to the left of the equal sign are parts of the space with a decrease on electron density while the areas in blue are gains in electron density.

$$\Delta\rho(\vec{x}) = \rho(\vec{x})_{s+ads} - \left(\rho(\vec{x})_s + \sum_{ads}\rho(\vec{x})_{ads}\right) \tag{4.2}$$

To gain an understanding of the potential reactivity of the different surfaces studied, the local density of states was calculated by projecting the plane wave expansion into a linear combination of pseudo-atomic orbitals. All simulations and data analysis were performed with the pw.x program and post processing utilities that are part of the quantum ESPRESSO package[75]. The visualizations were obtained with VMD[76] with the exception of Figure 2.1 were xcrysden[77] was used. All programs used in this dissertation are free and provided under the gnu license.

.

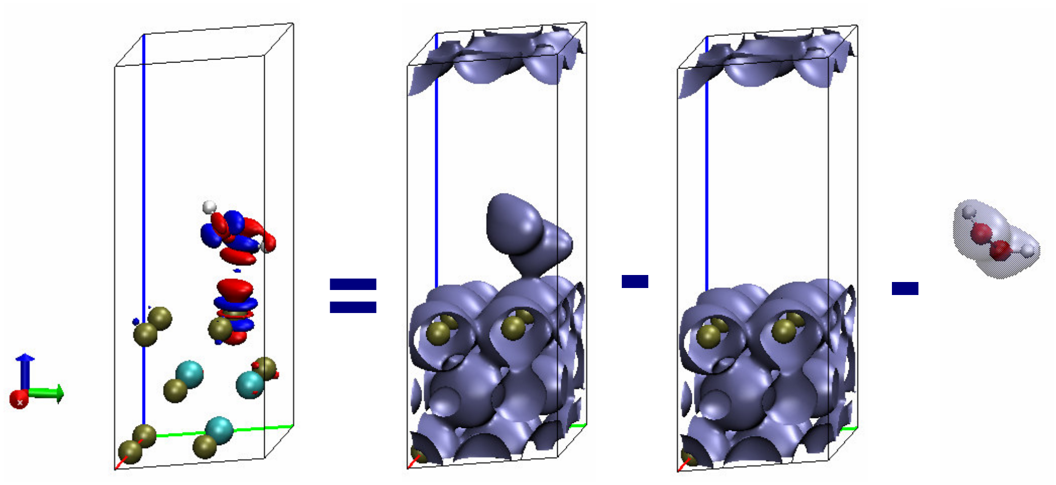

Fig. 4.1. Graphical representation of the process of taking differences in electron densities.

.

5. SURFACE CHARACTERIZATION

> Almost any English person would accept bully as a
> synonym for fascist.
> - George Orwell

5.1. Introduction

The presence of a second component in a pure metal will affect its electronic and structural properties. The presence of adsorbates will also result in changes on the surface characteristics. These changes are summarized in Figure 5.1.

Surface changes due to alloying and interaction with the environment

- Ensemble effects: due to the presence of one-component islands on the surface.
- Structural effects: changes on the surface geometry because of the presence of the extra components.
  Surface reconstruction: is a change in surface structure due to adsorbed species.
- Electronic effects: modification of the reactivity due to the presence of the solute compared with the pure component.

Fig. 5.1. Classification of changes a surface experiences upon alloying and when interacting with adsorbates.

The first type of change accounts for the possibility of one of the component in the alloy to segregate forming islands on the surface. This segregation might also occur if one of the components exhibits a different reactivity or solubility. For example, in a strongly acid environment giving place to skin structures where the more noble metal remains in the surface while the most reactive species dissolves into the solution.

The structural effects appear for example as changes in the bonding distances in the metal atoms. These distance changes also affect the band structure of the material since changes in lattice constant will change the lattice constant in reciprocal space, resulting in band structure changes. Xu, Ruban and Mavrikakis[53] has analyzed the effects of surface contraction on adsorption energies on transition metal surfaces. Hoffmann[39] has given a simple and clear explanation of the same effect using a one dimensional infinite chain of hydrogen atoms by analyzing the resulting band structures upon changes on bonding distances.

Finally, electronic structural changes other than those due to lattice contraction or expansion result from chemical interactions between the alloy components and will also result in changes in the location of the density of states with to respect to the Fermi level, affecting the reactivity of the surface.

5.2. Surface Structure, Changes Due to Alloying and Adsorbed Species

Solid platinum and palladium are metals with an fcc type of Bravais structure with observed lattice constants of 3.92 Å and 3.89 Å respectively. The first change that we will analyze in a surface is its contraction or expansion due to alloying. Lattice constants of different $Pt_xM_{(1-x)}$ and $Pd_xM_{(1-x)}$ solids were calculated by variable cell calculations using the Wentzcovitch damped dynamics algorithm[78]. In Table 5.1 we see that in general the calculation with the PBE functional gives a lattice constant for the pure metals that is expanded about 2% when compared with experiment. We should note the lattice contraction in the Co and Fe alloys compared with the pure Pt and Pd.

To study surface relaxation we used a four layer slab with the bottom two layers having interatomic distances fixed at their bulk distances values. In Figure 5.2, we can see the relaxation for the PdCo clean surface and the case when oxygen is adsorbed in the fcc hollow site. In all four surfaces, the relaxation behavior was similar. For example, we found that for the stronger of the interacting species (atomic oxygen on the fcc hollow site) on Pt(111) the calculated adsorption energy was –3.73 eV for the unrelaxed three layer surface model used here, and –3.70 eV for the unrelaxed 4 layer model while the model four-layer surface in which we allowed the two top layers to relax the adsorption energy calculated was –3.89 eV. Clearly, the resulting differences are quite

.

large (about 0.14 eV) but it tends to cancel from surface to surface, giving rise to the same trends. It is also much lower in adsorbate with weaker interactions with the surface.

Table 5.1.

Lattice constants for Pt, Pd and its alloys from different sources.

System	Lattice Constant (Å, this work)	Lattice Constant (Å, calc. from references)	Lattice Constant (Å, experimental)
Pt	4.00	4.00[53]	3.92
$Pt_{0.75}Co_{0.25}$	3.91	3.92[53]	3.85[79]
$Pt_{0.75}Fe_{0.25}$	3.94	3.94[53]	3.87[80]
Pd	3.93		3.89
$Pd_{0.75}Co_{0.25}$	3.85		3.82[81]
$Pd_{0.75}Fe_{0.25}$	3.88		

In Figure 5.2 we show the result of different geometry optimization runs where the first two layers of a four layer surface were allowed to relax. In the clean Pt(111) case there is a slight contraction in the second layer, while the first remained with the PBE bulk lattice constant. We note that some authors report slight expansion on the first layer probably as a result of using a different starting lattice constant since the differences are minor. On the other hand, on the clean bimetallic surfaces we find that the contraction is more noticeable in the second layer while in the first layer the behavior is less predictable for the Pd – Co. This probably results from broken symmetry due to the distribution of the underlying Co atoms. When oxygen is adsorbed into the fcc hollow site of the pure Pt surface the triangle formed by the Pt atoms underneath the O rotate, keeping the interatomic distance constant (2.93 Å) while the interlayer distance consequently shows two expansions and one contraction. The second layer shows contraction for all atoms when there is an expansion in the first layer and vice versa. The

.

analysis of the less predictable relaxation behavior in the PdCo alloy is similar to the one described above for the clean surface.

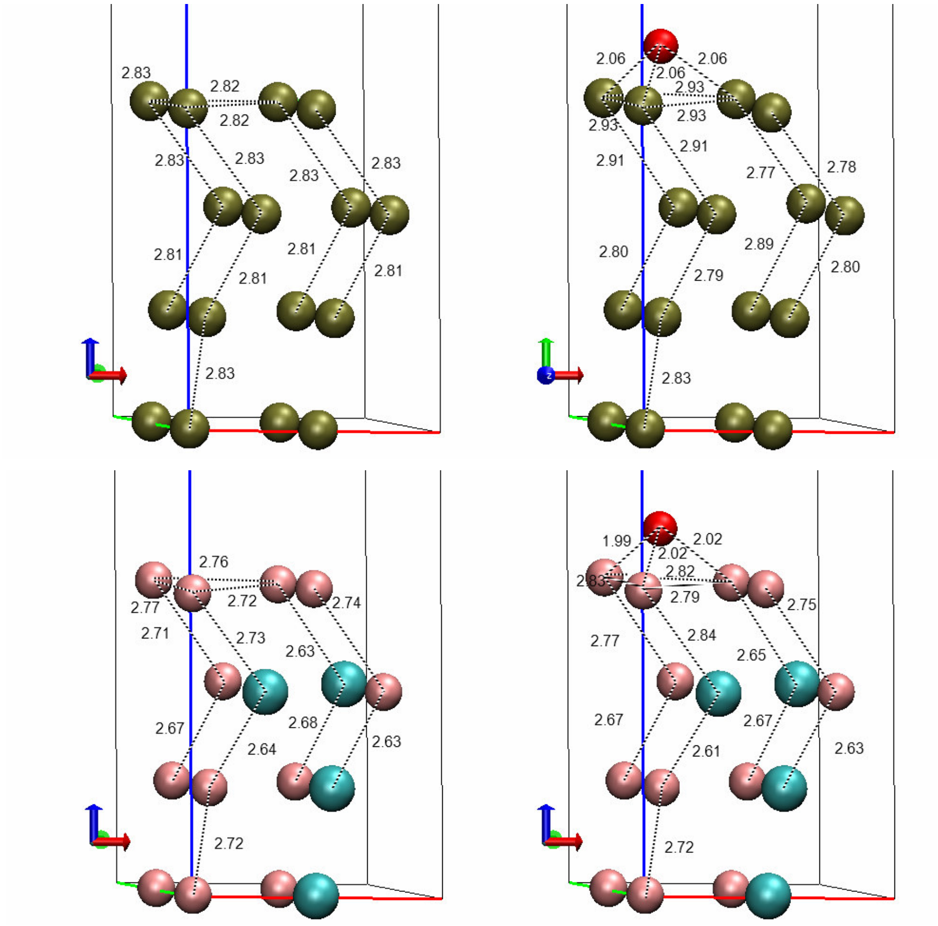

Fig. 5.2. Surface relaxation on the Pt (111) and PdCo alloys. Both the clean surface and the one with oxygen adsorbed in the fcc hollow site is shown. All distances are in angstroms.

.

5.3. Electronic Structure of Transition Metal Surfaces

Self-consistent field calculations in the Pt, Pd, $Pt_{0.75}Co_{0.25}$ and $Pd_{0.75}Co_{0.25}$ systems demonstrated the different magnetic properties of these alloys. While Pt and Pd are non-magnetic, their Co alloys are ferromagnetic with a calculated total magnetization per unit cell containing 12 atoms (9 Pt or Pd atoms and 3 Co) of 10.29 Bohr mag and 9.78 Bohr mag in the $Pt_{0.75}Co_{0.25}$ and $Pd_{0.75}Co_{0.25}$ cases respectively.

The surface electronic structure of the various transition metal surfaces is more easily understood and analyzed after localizing the electronic states via projection of the plane waves basis sets into pseudo atomic orbitals. The usefulness of the charge population analysis in a plane wave framework has been discussed in the literature. Segall et al.[82] found that the projection and Mulliken charge population analysis can be successfully used as a measurement of the covalency of the system. Table 5.2 shows the charge population analysis for the $Pd_{0.75}Co_{0.25}$ surface. The spilling parameter measures how well the plane wave eigenfunctions project into the pseudoatomic orbitals, a value of 0 indicating that the projection is perfect while s = 1 means that the plane wave eigenfunctions and the pseudoatomic orbitals are orthogonal[83]. In this case it was calculated to be s=0.0018. We must remember that since we are dealing with pseudoatoms the total charges shown are close to the total number of valence electrons, i.e. 10 electrons for an isolated Pd atom with an electronic structure [Kr] $4d^{10}$ and 9 for Co atoms with electronic structure [Ar] $3d^7$ $4s^2$. We see that the main contributors to the magnetism in the surface are the Co atoms with a magnetic moment averaging about 2.2 Bohr mag (nearly a triplet in chemistry terminology) per atom, much higher than the 0.2 Bohr mag per atom observed in Pd. The projection into localized states also allows us to discover the level of occupancy for the different atoms on the clean surface and when interacting with the adsorbates. An idea of the occupancy in the typical solid environment is also useful for the creation and testing of the pseudopotentials, since they allow us to find and use electronic states that are closer to that found under more realistic conditions than the ground state for the isolated atom.

.

Table 5.2.

Population analysis for the clean $Pd_{0.75}Co_{0.25}$ (111) surface.

Atom #	Layer #	Type	Spin	CHARGES			
				s	p	d	s + p + d
1	3 (top)	Pd	Up	0.1547	0.2317	4.7220	5.1084
			Down	0.1565	0.2419	4.5053	4.9037
			Up+Down	0.3113	0.4736	9.2273	10.0122
2	3 (top)	Pd	Up	0.1531	0.2339	4.7471	5.1341
			Down	0.1580	0.2406	4.4702	4.8688
			Up+Down	0.3110	0.4746	9.2173	10.0029
3	3 (top)	Pd	Up	0.1530	0.2339	4.7471	5.1340
			Down	0.1580	0.2406	4.4703	4.8689
			Up+Down	0.3110	0.4775	9.2174	10.0029
4	3 (top)	Pd	Up	0.1544	0.2323	4.7258	5.1126
			Down	0.1594	0.2419	4.7971	4.8983
			Up+Down	0.3138	0.4742	9.2229	10.0109
5	2 (middle)	Pd	Up	0.1286	0.3047	4.4791	5.2125
			Down	0.1444	0.3251	4.3859	4.8554
			Up+Down	0.2730	0.6298	9.1615	10.0679
6	2 (middle)	Pd	Up	0.1286	0.3047	4.7791	5.2124
			Down	0.1444	0.3551	4.3859	4.8554
			Up+Down	0.2730	0.6298	9.1650	10.0679
7	2 (middle)	Co	Up	0.1642	0.4748	4.8902	5.5292
			Down	0.1653	0.5082	2.6588	3.3323
			Up+Down	0.3295	0.9830	7.5490	8.8615
8	2 (middle)	Co	Up	0.1611	0.4699	4.8913	5.5224
			Down	0.1672	0.5157	2.2209	3.3533
			Up+Down	0.3282	0.9857	7.5618	8.8757
9	1 (bottom)	Pd	Up	0.1532	0.2331	4.7787	5.1651
			Down	0.1701	0.2589	4.4368	4.8657
			Up+Down	0.3233	0.4920	9.2155	10.0307
10	1 (bottom)	Pd	Up	0.1550	0.2310	4.7645	5.1506
			Down	0.1685	0.2594	4.4579	4.8858
			Up+Down	0.3235	0.4904	9.2224	10.0364
11	1 (bottom)	Pd	Up	0.1532	0.2331	4.7787	5.1651
			Down	0.1701	0.2589	4.4368	4.8657
			Up+Down	0.3233	0.4919	9.2155	10.0308
12	1 (bottom)	Co	Up	0.2061	0.3885	4.8855	5.4801
			Down	0.1959	0.4150	2.7027	3.3136
			Up+Down	0.4020	0.8035	7.5883	8.7937

Figure 5.3 shows the localized density of states vs. the energy (referred to the Fermi level of the metal or alloy calculated by the model) of the d-band in the surface Pd and Pt atoms for all surfaces studied in this work. The location of the first moment of the d-band structure (the d-band center) is also indicated. The d-band center is located 2.06 eV below the Fermi level in the $Pd_{0.75}Co_{0.25}$ surface, 1.88 eV for the Pd surface, 2.36 eV for Pt, and 2.49 eV for $Pt_{0.75}Co_{0.25}$. If the d-band model holds for these metals the strengths of the adsorbate – surface interactions should be in increasing order: PtCo < Pt < PdCo < Pd. An analysis of adsorption energy values in the Tables in Section 6 shows that the agreement is excellent. Notice also the difference in density of states for spin up and down in the magnetic cases. This effect is even more noticeable for the subsurface Co atoms (not shown here).

.

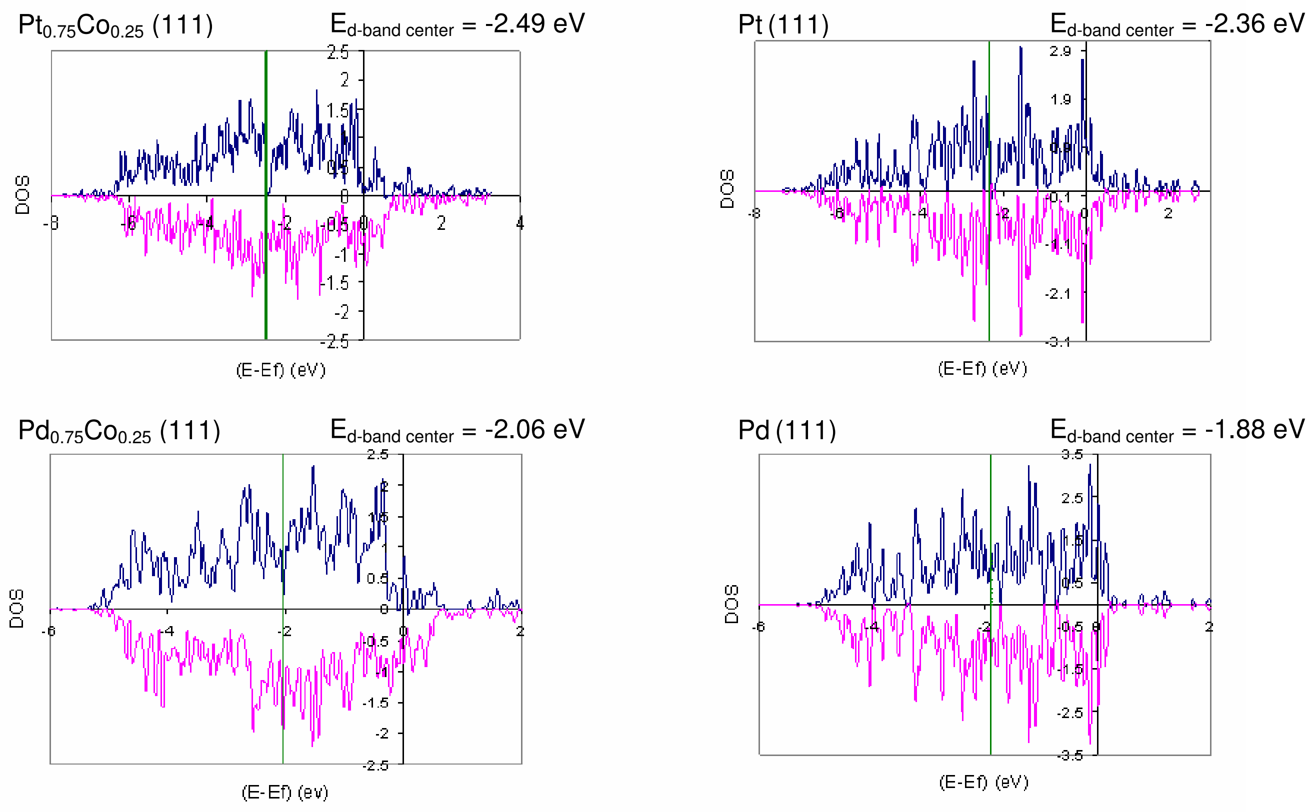

Fig. 5.3. d-band density of states for surface Pt or Pd atoms in the $Pd_{0.75}Co_{0.25}$, Pt, $Pd_{0.75}Co_{0.25}$ and Pd alloys.

6. OXYGEN ELECTROREDUCTION ON WATER-FREE SURFACES

> As soon as questions of will or decision or reason or choice
> of action arise, human science is at a loss.
> - Noam Chomsky

6.1. Introduction

In the last few years, the quest towards a hydrogen-based energy economy has intensified the interest for effective and less expensive catalysts for fuel cell applications. Due to its slow kinetics, alternative catalysts for the oxygen electro-reduction reaction (OERR) are being actively researched. Platinum alloys with different transition metals (for example: Ni, Co and Fe) have shown improved activity over pure Pt[25, 32, 84] in acid electrolytes. The design of a Pt-free catalyst is also highly desirable and different alternatives including metalloporphyrins[23] and Pd-based catalysts are being researched.[85-87] Pd-based catalysts constitute an attractive alternative to Pt alloys in fuel cell applications, not only because of lower costs but also because of their lower reactivity of towards methanol oxidation, which is important for improved methanol crossover tolerance in direct methanol fuel cells[37].

6.2. Analysis of the Intermediates of the Oxygen Reduction Reaction

6.2.1. Atomic and Molecular Oxygen

Dioxygen dissociation on Pt (111) is a thermally activated process that occurs above 150 K and involves chemically adsorbed precursors. The existence of these precursors has been verified both experimentally and theoretically[88]. Our studies of O_2 adsorption on the different (111) surfaces are in agreement with the existence of such precursors. Local minima on the potential energy surface were found for initial configurations of O_2 parallel to the surface, while the studied vertical orientation was not bonded to the surface. The reference calculation for oxygen in the gas phase yielded a triplet as the most stable electronic structure with a O–O bonding distance of 1.23 Å and a dissociation energy of 5.81 eV. Figure 6.1.b shows O_2 adsorbed on the Pd skin surface of the $Pd_{0.75}Co_{0.25}$ alloy, as well as the changes in electron density upon adsorption. It is observed that there is a decrease in the electron density in the O–O bond region and an electron flow from the surface to the antibonding π states of each O atom. Qualitatively, similar changes in the electronic density on O_2 adsorption are obtained for a Pt(111) surface. These are in excellent agreement with previously reported calculations on a Pt surface[51]. The bond elongations signaling weakening of the O–O bond in all studied surfaces are indicated in Table 6.1. The bond length value of 1.37 Å is in good agreement with experimental reports of the superoxo state on Pt(111) surfaces[89]. The interpretation of Equation 4.2 should be carefully analyzed in some cases. For some adsorbates, due to symmetry considerations there are several possible ways to calculate this difference. The clearer example is in the case of isolated atoms with non symmetrical electron densities (see Fig. 6.2). In this special case, this difference will depend on the orientation of the electron cloud of the isolated atom taken as a reference. This is the case of the oxygen atom. Nevertheless in this case, analysis of results taken with the default orientation is in qualitative agreement with that found in the hydroxyl case, where orientation is well defined since the orientation of the orbitals in the isolated reference radical is unambiguously determined by the orientation of the atoms in the adsorbed one.

.

Table 6.1.

DFT calculated dioxygen adsorption energies. The distance between the closest metal atom to each oxygen is tabulated together with the O–O bond distance.

System	ΔE (eV)	distances (Å)		
		O1-M1	O2-M2	O-O
$Pt\text{-}O_2$	–0.431	2.06	2.07	1.37
$Pt_{0.75}Co_{0.25}\text{-}O_2$	–0.216	2.14	2.17	1.33
$Pd_{0.75}Co_{0.25}\text{-}O_2$	–0.408	2.07	2.08	1.33
$Pd\text{-}O_2$	–0.715	2.01	2.02	1.35

Table 6.2.

DFT calculated oxygen adsorption energies and distances. In the hollow cases we report the distances to the three closest surface metal atoms.

System (site)	ΔE (eV)	distances (Å)		
		O-M1	O-M2	O-M3
Pt-O (fcc hollow)	–3.727	2.08	2.08	2.08
Pt-O (hcp hollow)	–3.316	2.11	2.11	2.11
Pt-O (top)	–2.492	1.87		
$Pt_{0.75}Co_{0.25}$-O (fcc hollow)	–3.490	2.1	2.1	2.09
$Pt_{0.75}Co_{0.25}$-O (hcp Co-hollow)	–2.995	2.13	2.14	2.09
$Pt_{0.75}Co_{0.25}$-O (hcp hollow)	–2.855	2.09	2.09	2.15
$Pd_{0.75}Co_{0.25}$-O (fcc hollow)	–3.778	2.02	2.02	2.03
$Pd_{0.75}Co_{0.25}$-O (hcp Co-hollow)	–3.473	2.03	2.03	2.01
$Pd_{0.75}Co_{0.25}$-O (hcp hollow)	–3.464	2.01	2.02	2.03
Pd-O (fcc hollow)	–4.153	1.99	1.99	1.99
Pd-O (hcp hollow)	–3.962	2.01	2.01	2.01
Pd-O (top)	–2.646	1.8		

.

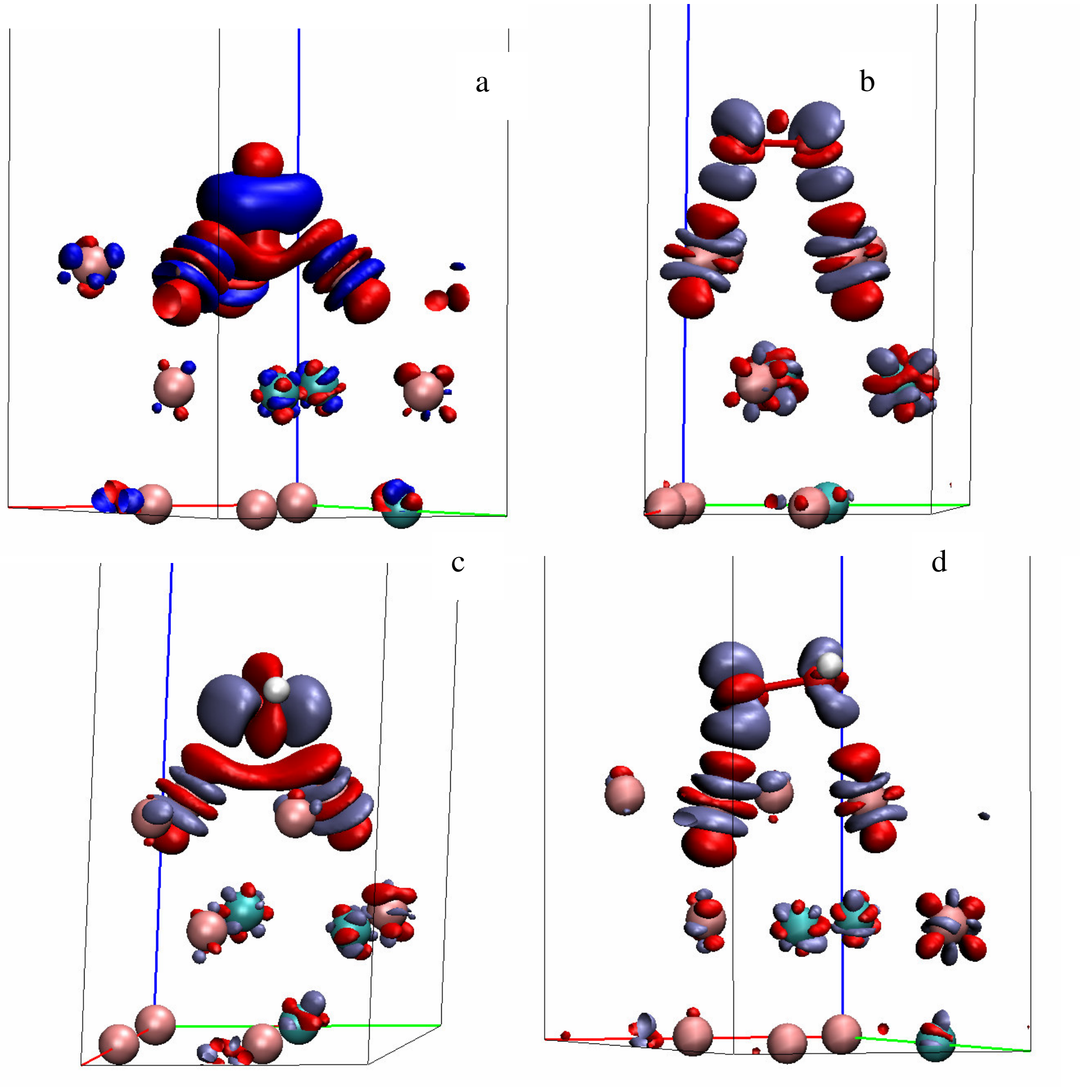

Fig. 6.1. Electron density differences upon adsorption calculated according to Equation 4.2, for (a) atomic oxygen, (b) dioxygen, (c) hydroxyl and (d) hydroperoxyl on the $Pd_{0.75}Co_{0.25}$ (111) surface. Pd atoms are in pink, Co atoms in light blue, oxygen in red and hydrogen in white. Positive electron density differences are in ice blue and negative electron density differences are in red. $\Delta\rho$ isosurfaces were calculated at +/– 0.006 e/au^3.

.

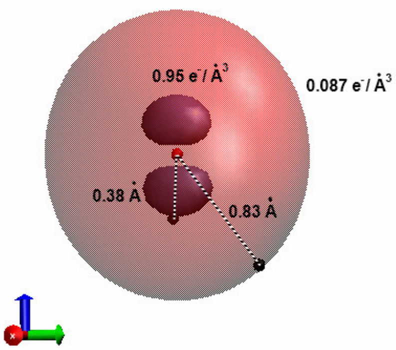

Fig. 6.2. Two iso-density surfaces in the isolated oxygen atom.

In all surfaces in this study, the preferred adsorption site for atomic oxygen is found to be the *fcc* hollow site (in good agreement with previously reported results[48]), followed by the *hcp* hollow, and then the top site (Table 6.2). O adsorbed on a top site becomes unstable on alloy surfaces, in all cases it slips to a neighbor *hcp* hollow position with an underlying Co atom in the second surface layer. The energetic difference between adsorption in both hollow sites (and thus the barriers for O surface diffusion) are also altered by the presence of second layer Co atoms. Indeed, in both alloys this difference is higher than that of the pure metal, going from 0.411 eV for pure Pt to 0.635 eV for $Pt_{0.75}Co_{0.25}$ alloy, and from 0.192 eV on Pd to 0.314 eV on $Pd_{0.75}Co_{0.25}$ alloy. Due to the strong O-metal bonding, the changes in electron density depicted in Figure 6.1.a are largest among the different adsorbates showing increased electronic density along a plane parallel to the surface and depleted electronic density along a line perpendicular to the surface, with changes on the surface metal atoms along the metal-adsorbate bonds. These features essentially remain for all adsorbates, i.e. for symmetry axes for electronic density changes parallel and perpendicular to the surface for the adsorbate and along metal-adsorbate bonds.

.

6.2.2. Hydroxyl (OH)

OH is perhaps one the most important OERR intermediates. Experimental evidence suggests that it adsorbs strongly on the catalyst surface, blocking active sites[84]. Its degree of interaction with different transition metal surfaces is an important indication of their efficacy towards oxygen reduction.

From the calculations performed it was observed that on Pt-based surfaces the preferred adsorption site is on top, while the preferred adsorption site is bridge for Pd surfaces. The top site is no longer stable on the Pd atoms of $Pd_{0.75}Co_{0.25}$ alloy (similarly to the atomic oxygen case, the top OH slips to neighbor bridge sites). The adsorbate is slightly displaced from the top position in $Pt_{0.75}Co_{0.25}$ but is still a stable local minimum. Energies and bond distances are given in Table 6.3.

Figure 6.1.c shows the geometry and electronic changes for OH adsorbed on the Pd surface of the $Pd_{0.75}Co_{0.25}$ alloy. Qualitatively the changes in electronic density are similar to those for adsorbed atomic oxygen (Figure 6.1.a), although they are less dramatic changes due to the lower binding strength.

At a higher OH concentration (half of a monolayer obtained as a product of the H_2O_2 dissociation on the surfaces), a hydrogen bond is formed between adsorbed neighboring OH species. This further stabilizes the hydroxyl groups, giving adsorption energies per OH that are lower than at low coverage by an amount close to the hydrogen bonding energy in water (23.3 KJ/mol or about 0.24 eV see for example ref.[90]). Binding energies and geometries for the 0.5 OH adsorbed monolayer are further discussed in section 6.2.4 where we study H_2O_2 dissociation.

.

Table 6.3.

DFT calculated hydroxyl adsorption distances and energies. In the bridge adsorption cases the reported distances are for the two closest surface metal atoms.

		distances (Å)		
System (site)	ΔE (eV)	O-M1	O-M2	O-M3
Pt-OH (top)	–2.081	2.02		
Pt-OH (bridge)	–1.989	2.22	2.21	
$Pt_{0.75}Co_{0.25}$-OH (top)	–1.870	2.05		
$Pt_{0.75}Co_{0.25}$-OH (bridge)	–1.791	2.24	2.27	
$Pd_{0.75}Co_{0.25}$-OH (top)	—			
$Pd_{0.75}Co_{0.25}$-OH (bridge)	–2.199	2.19	2.17	
Pd-OH (top)	–2.173	1.97		
Pd-OH (bridge)	–2.357	2.14	2.13	

6.2.3. Hydroperoxyl (HO_2)

In all calculated Pt and Pd-skin cases, HO_2 is stable and no dissociated form is found when starting from an undissociated initial condition. To calculate the binding energies, the HO_2 radical is taken as a reference in the gas phase, with a O–O bonding distance of 1.35 Å, O–H distance of 0.99 Å, and O–O–H angle of 104.96°. After adsorption, the molecule tilts on top of two metal atoms. This is due to the weaker interaction of the OH side of the molecule with the surface. The adsorption energies are listed in Table 6.4. Figure 6.1.d shows the geometry of adsorption over the Pd surface of the $Pd_{0.75}Co_{0.25}$ alloy, with an electron density difference isosurface of the calculated from to Equation 4.2. Not surprisingly, the features of this $\Delta\rho$ plot (Figure 6.1.d) are comparable to the O_2 case: that is, there is an electron density gain in the antibonding π orbital associated with each oxygen atom, which is lower in the end of the molecule bonding to hydrogen because of the stability of the O–H covalent bond.

.

Table 6.4.

DFT calculated HO_2 adsorption distances and energies. The last column shows the O–O distance in the adsorbate.

		distances (Å)		
System	ΔE (eV)	O1-M1	O2-M2	O-O
Pt-HO_2	–1.043	2.86	2.06	1.43
$Pt_{0.75}Co_{0.25}$-HO_2	–0.881	2.9	2.08	1.43
$Pd_{0.75}Co_{0.25}$-HO_2	–0.973	2.41	2.04	1.46
Pd-HO_2	–1.218	2.32	2.01	1.47

6.2.4. Hydrogen Peroxide (H_2O_2)

The most stable electronic configuration for H_2O_2 is a singlet with bond lengths 1.47 Å for O–O and 0.98 Å for O–H, angles about 100° for H–O–O and dihedral angle about 112°. When placed over a surface at about 2 Å in vacuum, dissociation is observed in all cases, whereas when placed above 2.6 Å the molecule adsorbs without dissociation tilted with one of its oxygen atoms over a top position. Dissociation energies are given in Table 6.5. Once dissociated, two OH species are observed in two possible configurations: one where both OH radicals are adsorbed on top of metal atoms and another where one OH adsorbs on top while the other is in a near-hollow position. On the Pd surface of the $Pd_{0.75}Co_{0.25}$ alloy, a top-top configuration seems to be slightly preferred (Table 6.5). Similar results have been reported on Pt(111)[54]. In both cases, the adsorbed OH rotates, forming a hydrogen bond with its neighbor OH radical. The hydrogen bond distances are also given in Table 6.5.

.

Table 6.5.

DFT calculation of H_2O_2 dissociation to two adsorbed OH radicals.

System (site 1- site 2)	$\Delta E^{(1)}$ (eV)	$\Delta E^{(2)}$ (eV)	distances (Å)				H-bond dist (Å)
			O1-M1	O2-M2	O2-M3	O2-M4	
Pt-2OH (top-top)	–2.056	–2.294	2.02	2.02			1.87
$Pt_{0.75}Co_{0.25}$-2OH (top-top)	–1.668	–2.100	2.04	2.04			1.78
$Pd_{0.75}Co_{0.25}$-2OH (top-top)	–1.795	–2.163	2	1.99			1.85
$Pd_{0.75}Co_{0.25}$-2OH (top-hollow)	–1.777	–2.154	2.01	2.09	2.31	2.74	2.14
Pd-2OH (top-top)	–2.144	–2.338	1.97	1.97			1.95

$\Delta E^{(1)}$ is the binding energy calculated according to Equation 4.1 with n =1 and taking E_{H2O2} as E_A, whereas $\Delta E^{(2)}$ is calculated with n = 2 and E_{OH} as E_A. The values of $\Delta E^{(2)}$ may be compared with those in Table 6.3 to quantify the stabilization due to hydrogen bonding . The last column in this Table gives the hydrogen bonding distance between neighboring hydroxyls.

6.3. Free Energy Profiles

Oxygen electroreduction in acidic media can occur through one or a combination of two different paths; a *direct* pathway that involves O–O bond breaking before a second proton is attached to the molecule and a *series* pathway that generates hydrogen peroxide as an intermediate. The two pathways that were also shown in the review section can be represented as[24, 25]:

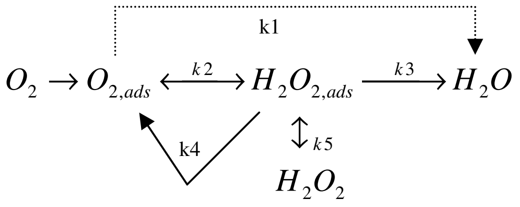

.

In this section we study two representative mechanisms of the OERR one for each pathway via generation of free energy profiles. Gibbs free energy changes for the elementary steps including zero point energies and entropies, and cell potential effects are estimated following the methodology introduced by Norskov et al.[63, 64]

The ΔG for the overall reaction on the hydrogen electrode scale is calculated to be 2.13 eV, making the theoretical results in error by about 14%, since the experimental value is 2.5 eV. This is in part attributed to the difficulties in modeling the O_2 electronic structure[64]. The results shown below, which introduce the electrode potential in the free energy profiles are based on the *calculated* ΔG for the overall reaction.

In Figure 6.3 we show a representation of a typical fuel cell. In this and the following section we will study the oxygen electroreduction mechanism and its dependence on the electrode potential.

The maximum theoretical electrode potential that the fuel cell can generate is given by the following thermodynamic relation:

$$\Delta G = -nFU \tag{6.1}$$

where:

n is the number of electrons involved in the redox reaction
F is the Faraday constant
U is the electrode potential

To characterize electrocatalyst behavior and the possible mechanisms for oxygen electroreduction three potentials are studied: the maximum thermodynamic potential U=1.23 V (or according to our calculations, and the value used for consistency, U=1.07), the case were the cell is at short circuit (that is, R=0 and U=0 V in Figure 6.2), and the potential under working conditions in normal fuel cell operation, U=0.78 V.

.

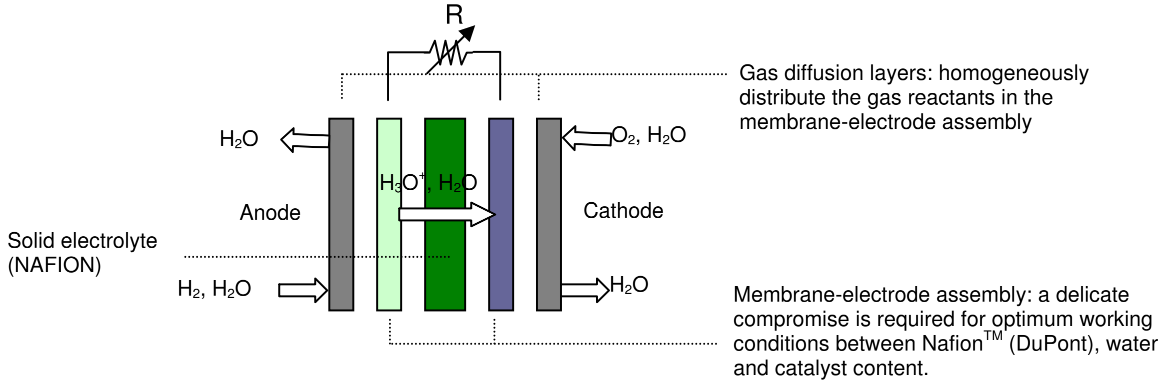

Fig. 6.3. Schematic representation of the PEM Fuel Cell main components.

All free energy profiles were calculated at pH =0. For other pHs the profiles should be corrected with an additional contribution to G as suggested by Norskov et al.[63] by:

$$G(pH) = -k \cdot T \ln[H^+] = k \cdot T \ln(10) \cdot pH \qquad (6.2)$$

Table 6.6.

Zero point energies and entropies for oxygen electroreduction intermediates[63]

Intermediate	ZPE (eV)	T*S (eV) T=300K
H_2	0.27	0.406
O_2	0.1	0.64
H_2O	0.56	0.59
H_2O_2	0.699	0.729
O*	0.07	0
O_2*	0.14	0
HO*	0.335	0
HO_2*	0.405	0

.

In Table 6.6 a compilation of values for zero point energies and entropies is shown for the different OERR intermediates. As an approximation, we assume that the same values for the zero point energies can be applied indistinctively to the four different surfaces.

The equations used to calculate the free energy profiles are developed in detail in the following two sections for mechanisms representative of the direct (2 e^-) and series (4 e^-) pathways. Finally, the last key assumption used in the procedure to build the free energy profiles is the fact that the anodic reaction:

$$H_2 \rightarrow 2H^+ + 2e^- \qquad (6.3)$$

occurs as much as to 10^7 times faster than the cathodic reaction we assume that H_2 and ($H^+ + e^-$) are in equilibrium.

6.3.1. A Direct Pathway Mechanism

A simple mechanism considered for to the *direct* pathway, where the O–O splits before the first protonation, is summarized by reactions 6.4 to 6.6. We note that in our models we assume that in reaction 6.4 dioxygen adsorbs and dissociates to give to oxygen radicals in neighboring fcc hollow sites. The barrier associated to O_2 dissociation and subsequent diffusion is not included in the profiles. Despite of its simplicity this mechanism has many advantages. It is simple but it captures many important characteristics of this reaction and it allows us to compare the resulting profiles with already published data see ref.[63]. In addition, trends on catalytic activity for the surfaces studied here will also be present in the mechanism studied in the next section. Figure 6.4 shows the ΔG profile for the cell at the equilibrium potential using this assumption.

.

$$\frac{1}{2}O_2 + * \rightarrow O* \tag{6.4}$$

$$O* + (H^+ + e^-) \rightarrow OH* \tag{6.5}$$

$$OH* + (H^+ + e^-) \rightarrow H_2O + * \tag{6.6}$$

The Gibbs free energy profiles were constructed following the Norskov procedure[63] as illustrated below for the series mechanism. Free energy values for the different OERR steps are labeled G_i and were calculated according to the following equations (see also Fig. 6.4):

$$G_1 = -\Delta G_{U=0} - 2 \cdot eU \tag{6.7}$$

$$G_2 = -\Delta G_{U=0} - 2 \cdot eU + \Delta G_4 \tag{6.8}$$

$$G_3 = -\Delta G_{U=0} - eU + \Delta G_4 + \Delta G_5 \tag{6.9}$$

$$G_4 = -\Delta G_{U=0} + \Delta G_4 + \Delta G_5 + \Delta G_6 \equiv 0 \tag{6.10}$$

where :

$$\Delta G_i = \Delta E_i + \Delta ZPE_i - T \cdot \Delta S_i \tag{6.11}$$

ΔE_i and ΔZPE_i can be calculated via Ab Initio techniques and ΔS_i can be obtained from thermodynamic tables. In this work ΔZPE_i and ΔS_i are from ref [63]. U is the cell potential, the number multiplying it is the number of electrons involved in that step, and $\Delta G_{U=0}$ is defined by Equation 6.11.

.

The surface with the highest d-band center, therefore the most reactive is Pd (111). It is the only one on which the current model predicts water dissociation (the evolution from right to left in Figure 6.4) at the cell equilibrium potential and at the oxygen coverage studied ($\theta = 0.25$). On the other hand, for Pt(111) at the equilibrium potential, and at oxygen coverage $\theta = 0.25$ in the absence of water, we find a slight uphill pathway for water dissociation. Norskov et al.[63] show a thermodynamic barrier for water dissociation at the cell equilibrium potential and $\theta = 0.5$, while the barrier becomes downhill at an unspecified low coverage. Based on their largest cell size, we assume that this corresponds to a value of $\theta = 0.167$. This is in good agreement with our results, which predict a thermodynamic barrier located between these two cases. The Pt surface of the $Pt_{0.75}Co_{0.25}$ alloy shows values of ΔG along the pathway that are above the Pt and $Pd_{0.75}Co_{0.25}$ surfaces, while the Pd surface which has the strongest bonds with the intermediates is lowest. Based solely on the data obtained on the profile the highest thermodynamic barrier for this reaction mechanism under the specific conditions (low oxygen coverage, no bulk water) is likely to be located at the first protonation (Equation 6.5).

.

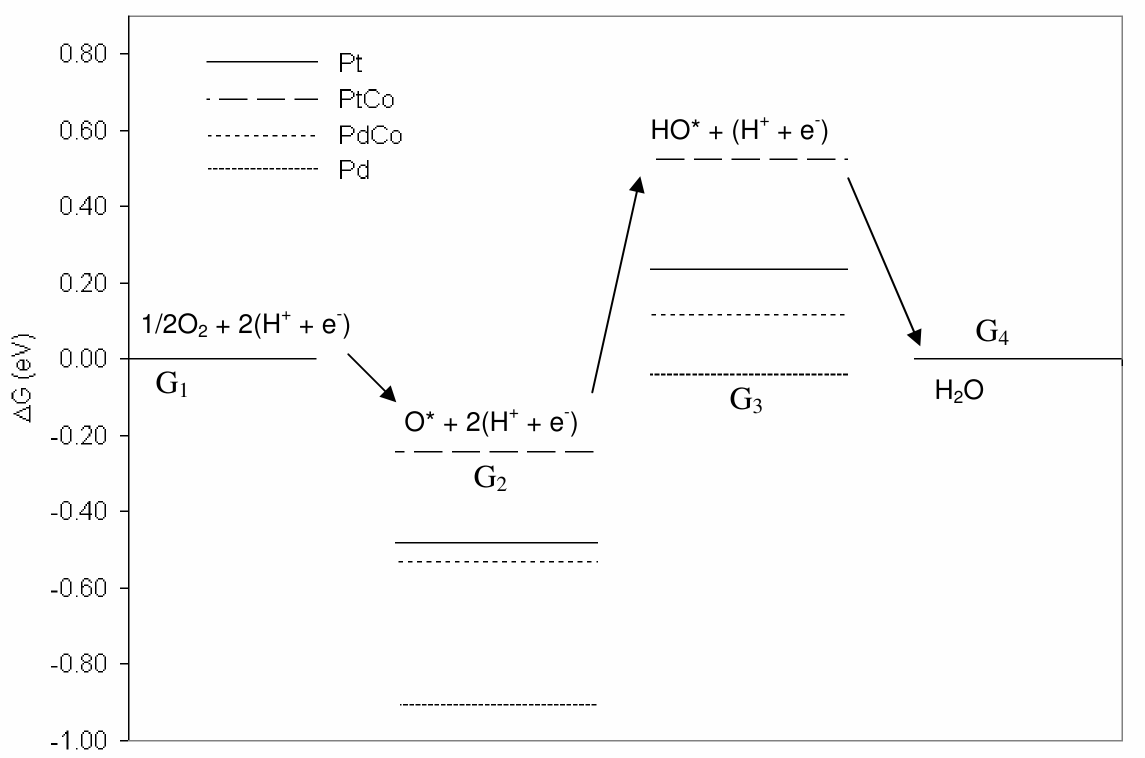

Fig. 6.4. DFT calculated Gibbs free energy profile for a *direct* mechanism of the OERR on Pt, $Pt_{0.75}Co_{0.25}$ and $Pd_{0.75}Co_{0.25}$, and Pd surfaces at the cell equilibrium potential.

.

6.3.2. A Series Pathway Mechanism

The Gibbs free energy profile for a series mechanism indicated by the chemical reactions 6.12 through 6.16 is shown in Figure 6.5 at U=1.07 V. In this mechanism we assume that H_2O_2 is unstable on all surfaces and thus the result of the second hydrogenation reaction is its immediate dissociation yielding two adsorbed hydroxyl groups.

$$O_2 + * \rightarrow O_2* \tag{6.12}$$

$$O_2* + (H^+ + e^-) \rightarrow HO_2* \tag{6.13}$$

$$HO_2* + (H^+ + e^-) \rightarrow H_2O_2* \rightarrow 2OH* \tag{6.14}$$

$$2OH* + (H^+ + e^-) \rightarrow H_2O + OH* \tag{6.15}$$

$$OH* + (H^+ + e^-) + H_2O \rightarrow 2H_2O + 2* \tag{6.16}$$

Proceeding in the same way as in Section 6.6.1 for the direct mechanism, values for the Gibbs free energy at each step of the four electron pathway were calculated as:

$$G_1 = -\Delta G_{U=0} - 4 \cdot eU \tag{6.17}$$

$$G_2 = -\Delta G_{U=0} - 4 \cdot eU + \Delta G_{6.12} \tag{6.18}$$

$$G_3 = -\Delta G_{U=0} - 3 \cdot eU + \Delta G_{6.12} + \Delta G_{6.13} \tag{6.19}$$

$$G_4 = -\Delta G_{U=0} - 2 \cdot eU + \Delta G_{6.12} + \Delta G_{6.13} + \Delta G_{6.14} \tag{6.20}$$

$$G_5 = -\Delta G_{U=0} - eU + \Delta G_{6.12} + \Delta G_{6.13} + \Delta G_{6.14} \tag{6.21}$$

$$G_6 = -\Delta G_{U=0} + \Delta G_{6.12} + \Delta G_{6.13} + \Delta G_{6.14} + \Delta G_{6.15} + \Delta G_{6.16} \equiv 0 \tag{6.22}$$

where :

$$\Delta G_i = \Delta E_i + \Delta ZPE_i - T \cdot \Delta S_i \tag{6.23}$$

.

ΔE_i and ΔZPE_i ΔS_i and U are the changes in energy, zero point energy, entropy and cell potential as given in Section 6.6.1.

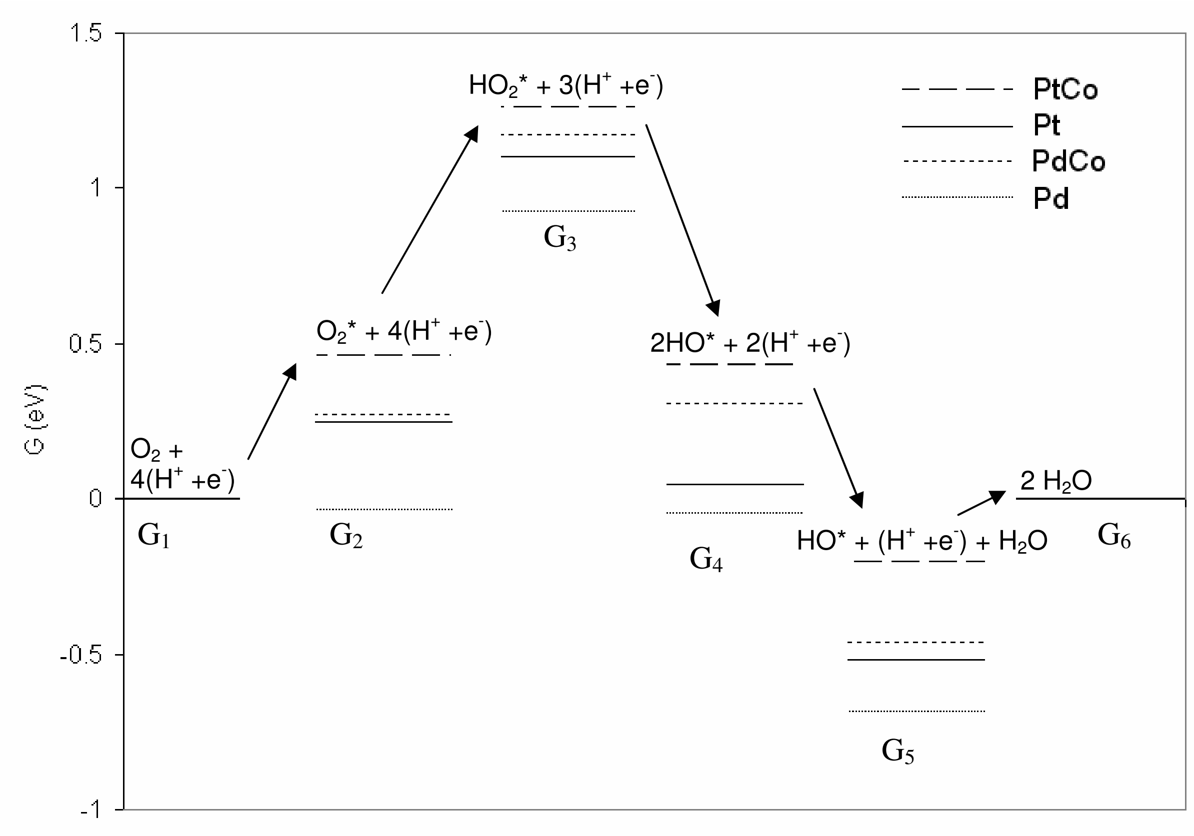

Fig. 6.5. DFT calculated Gibbs free energy profile for a possible *series* mechanism of OERR in Pt, $Pt_{0.75}Co_{0.25}$ and $Pd_{0.75}Co_{0.25}$, and Pd surfaces at the cell equilibrium potential.

.

At the U=1.07 V (Figure 6.5) there are a series of uphill thermodynamic barriers for the formation of water from hydrogen and oxygen. As in the first mechanism, the free energy profile under these idealized conditions indicates that the highest thermodynamic barrier is the first protonation (Equation 6.13). Reactivity trends similar to those in the *direct* mechanism are found among the various surfaces, in agreement with the d-band center model. The difference in values for the thermodynamic barriers in the two mechanisms is comparable, signaling that they both might be active and operating in parallel.

6.4. Conclusions

Binding energies of oxygen electroreduction intermediates and free energy profiles for *direct* and *series* reaction mechanisms on (111) surfaces of Pt, Pd, $Pd_{0.75}Co_{0.25}$ and $Pt_{0.75}Co_{0.25}$ indicate that the d-band model correctly predicts affinities towards the different ORR intermediates and reactivity trends on the studied surfaces. The study of the free energy profiles and the magnitude of the thermodynamic barriers in both mechanisms seem to favor the hypothesis that in the O_2 reduction mechanism to water they both might be operating in *parallel*. The highest thermodynamic barriers appear to be located in the first protonation process for both mechanisms when the system is studied at conditions of ¼ of a monolayer and in the absence of bulk water.

7. OXYGEN ELECTROREDUCTION ON WATER-COVERED SURFACES

All models are wrong, but some are useful.
- George E. P. Box

7.1. Introduction

In this section we repeat our studies of oxygen electroreduction intermediates by adding a surface layer of water that will interact with them, changing their properties. As a result of the increased degrees of freedom for the relaxation calculations a number of local minima for the different surfaces were expected. However, in general, the geometric characteristics obtained such as distances, orientations and bond distances in the adsorbate (e.g. O–O bond elongation in the hydrated intermediates) on the different surfaces were strikingly similar. This indicates that the source of variations in energy was purely electronic in nature. The nature of the bonding to the surface dominated by the location of the d band center for each alloy, and by the degree of weakening of the metal-metal bonds in the subsurface transition metal atoms as a result of the interactions with the adsorbate. In this section we analyze each of the intermediates, and we describe qualitative features; unless otherwise specified the observations regarding adsorbate geometry are common to all surfaces studied.

7.2. Analysis of the Intermediates of the Oxygen Reduction Reaction in Presence of Water

7.2.1. Water on Transition Metal Surfaces

To establish a reference, we calculated the optimized configurations of two small water clusters. The calculated O–O distance in the water dimer was 2.9 Å, the energy associated for breaking the hydrogen bond in the dimer was 0.22 eV. In the water trimer the O–O distance is shortened to about 2.77 Å, a value close to the metal-metal distances in the (111) surfaces studied (see Figure 7.1). The energy difference per water molecule

.

with respect to the isolated molecules in the trimer was calculated according to Equation 7.1 and found to be 0.23 eV.

$$\Delta E = \frac{1}{n}\left(E_{nH_2O} - n \cdot E_{H_2O}\right) \qquad (7.1)$$

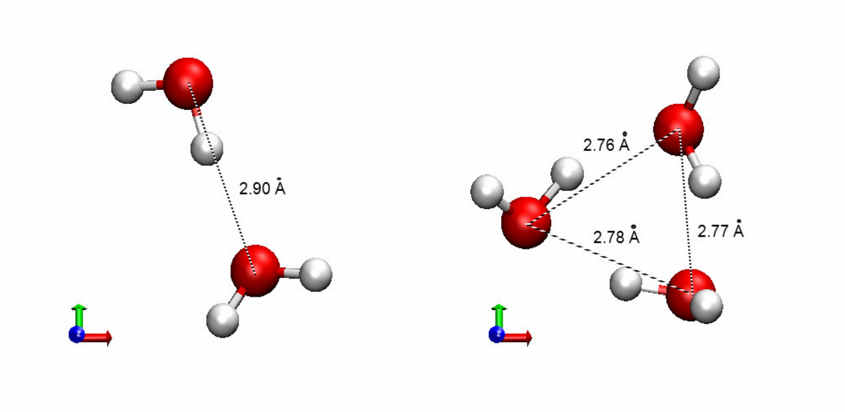

Fig. 7.1. Water dimer and trimer structures.

.

To study water interaction with the transition metal surfaces three different systems were constructed corresponding to different water coverages, going from $^2/_3$ of a monolayer (the saturation coverage) to ¼ of a monolayer. Water was observed to adsorb intact (i.e. without dissociation) on all surfaces studied at all surface concentrations. In Table 7.1 we report the adsorption energies calculated according to Equation 4.1 at different coverages. At the lowest water surface concentration studied ($\theta = 0.25$) water molecules were lying flat, with the plane defined by the three atoms parallel to the surface, with the oxygen atom on top of a surface (Pt or Pd) atom. The calculated adsorption energies ranged from –0.18 eV to –0.21 eV for Pt, $Pt_{0.75}Co_{0.25}$ and $Pd_{0.75}Co_{0.25}$ surfaces, while the Pd surface showed a higher value of –0.26 eV due to its relatively higher d-band center location. The projection of the delocalized plane wave into the pseudo atomic orbitals followed by a Lowdin charge distribution analysis shows a transfer of charge to the surface from the oxygen atom in the water molecule corresponding to about 0.15 e^- when compared with the charge distribution of water in the gas phase. The change in the amount of the charge transfer from one surface to another was minimal. Figure 7.2 shows the changes in electron density for a water molecule on the $Pd_{0.75}Co_{0.25}$ surface.

At $^2/_3$ of a monolayer we find a bilayer-like structure forming a hexagonal network with water adsorbing without dissociation, with a maximum distance between O atoms in the z direction of about 1 Å, and adsorption energy per water molecule of about 0.4 eV. As it was mentioned earlier different structures are obtained as the unit cell size is increased, for example some authors have reported dissociation into H_3O^+ and OH^- species on Pt (111) and the reader is referred to those works to complement this study at high water coverages[57, 91]. We will further discuss this problem when interpreting the results of the free energy profiles for the series mechanism.

Table 7.1.

Adsorption energy per water molecule at different surface concentrations.

System	ΔE (eV) θ = .75	ΔE (eV) θ = .5	ΔE (eV) θ = .25
$Pt_{0.75}Co_{0.25}$-H_2O	–0.40	–0.33	–0.18
Pt-H_2O	–0.41	–0.33	–0.19
$Pd_{0.75}Co_{0.25}$-H_2O	–0.41	–0.35	–0.21
Pd-H_2O	–0.46	–0.38	–0.26

7.2.2. Atomic and Molecular Oxygen

In studying changes in adsorption properties for atomic oxygen in the presence of water we focus our attention on the preferred fcc hollow adsorption site for the oxygen atom and we calculate the new energies and optimum structures on surrounding it by water. The values for the adsorption energies are listed in Table 7.2; the adsorption distances are slightly elongated in all cases compared with those found in vacuum simulations. The closest hydrogen from a neighbor water is located about 1.74 Å away for Pt and Pt based alloys, and about 1.7 Å for the corresponding Pd cases.

Table 7.2.

Adsorption energies for atomic oxygen in the fcc hollow site in the presence (ΔE_1) and absence of water (ΔE_2) at the surface.

System	ΔE_1 (eV)	O-M dist (Å)			ΔE_2 (eV)	O-M dist (Å)		
$Pt_{0.75}Co_{0.25}$-O (fcc Hollow)	–3.60	2.11	2.12	2.14	–3.49	2.1	2.1	2.1
Pt-O (fcc Hollow)	–3.80	2.10	2.11	2.14	–3.73	2.08	2.08	2.08
$Pd_{0.75}Co_{0.25}$-O (fcc Hollow)	–3.99	2.05	2.06	2.09	–3.78	2.02	2.02	2.03
Pd-O (fcc Hollow)	–4.31	2.02	2.03	2.05	–4.15	1.99	1.99	1.99

.

We calculated the difference in energy for each surface for the following reaction:

$$O^{*} + 2H_2O \rightarrow 2OH^{*} + H_2O \tag{7.2}$$

Reaction (7.2) can be used as a measure of the stability of the otherwise highly reactive oxygen radical on the different surfaces. Interestingly, water deprotonation is energetically downhill only on Pt and its alloy (ΔE_r equal to –0.3 eV and –0.08 eV for Pt and the $Pt_{0.75}Co_{0.25}$ alloy respectively), while the corresponding Pd materials stabilize the adsorbed oxygen sufficiently to make the reaction energetically uphill (ΔE_r equal to 0.24 eV and 0.48 eV for Pd and the $Pd_{0.75}Co_{0.25}$ alloy respectively). This qualitative change from Pt-based to Pd-based surfaces indicates one of the problems of Pd, i.e., its tendency to form an oxide layer over the surface under fuel cell operating conditions, diminishing its performance over time.

Table 7.3.

Adsorption energies for dioxygen in the presence of water on transition metal surfaces.

System	ΔE_1 (eV)	O-O dist (Å)	ΔE_2 (eV)	O-O dist (Å)
$Pt_{0.75}Co_{0.25}$-O_2	–0.47	1.45	–0.18	1.41
Pt-O_2	–0.83	1.47	–0.49	1.41
$Pd_{0.75}Co_{0.25}$-O_2	–0.72	1.42	–0.51	1.41
Pd-O_2	–1.15	1.44	–0.92	1.40

The calculated O–O bond distance for a O_2 molecule in vacuum was found to be 1.23 Å. ΔE_1 (eV) Ads. Site: (top-top) ΔE_2 (eV) Ads. Site: (top-bridge) both cases in presence of water.

.

In agreement with observations and theoretical vacuum calculations, we found, two different adsorbed O_2 species with different accompanying water; their energies and O–O bond distances are given in Table 7.3. The first with lowest energy is flat configuration with the O_2 adsorbed in a top-top site, i.e., with each oxygen atom near but not exactly in a top position. This is also shown in Figure 7.2 in a four-cell side view (right) and in a single cell view (left) where the differences in electron densities with respect to the isolated adsorbates and clean surface are given. The electron density difference also shows the complexity in the electronic structure introduced by the presence of the solvent and its interaction with the adsorbate. To fully appreciate this difference the reader is referred to the corresponding figure in vacuo previously published[92]. The second type of adsorbed O_2 is with an oxygen atom on top and the other on a bridge position. In this case, the adsorbates adopt a bilayer structure instead of the flat monolayer previously found.

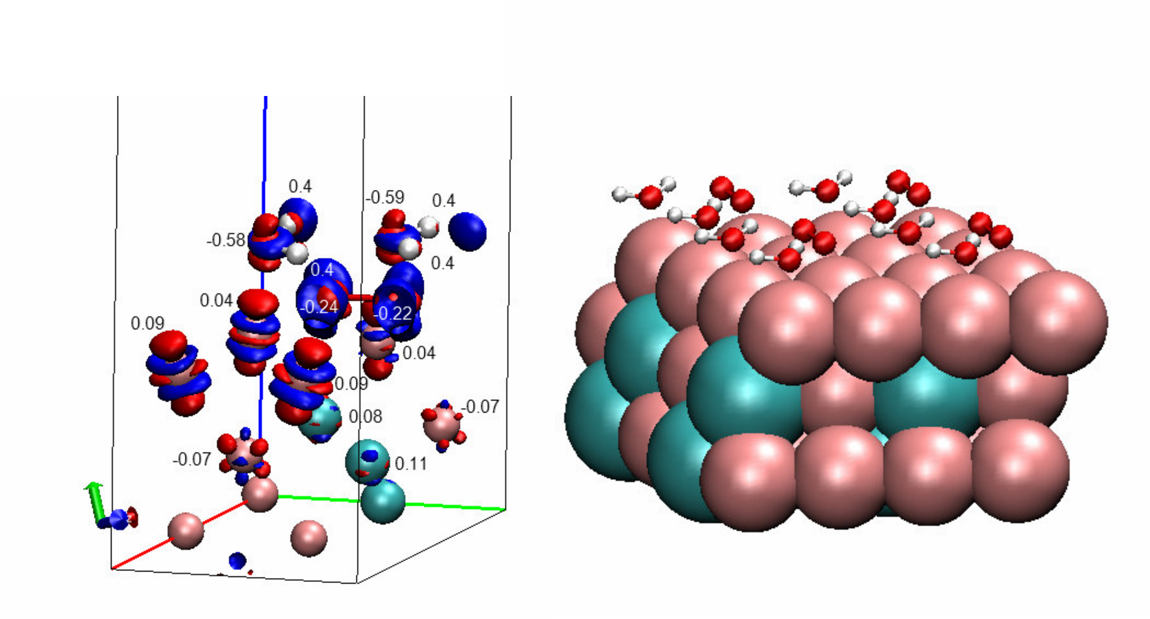

Fig. 7.2. Left: Molecular oxygen adsorbed in the presence of water on the $Pd_{0.75}Co_{0.25}$ surface. Lowdin charges for the adsorbates and the first two layers are indicated. $\Delta\rho$ surfaces are placed at +/– 0.01 $e^{-}/Å^{3}$. At the right, a four cell view.

.

7.2.3. Hydroxyl (OH)

The hydroxyl case is a clear example where water is expected to exert an important impact in adsorption conformation and energetics (Table 7.4). Not surprisingly the difference in energy (about 0.6 eV) between the cases where water was present or not is highest among all intermediates studied. We analyzed the hydroxyl case on all four surfaces with OH adsorbed on the top position and with different water coverages, finding that the hydrogen bonding distance varied from 1.52 Å on $Pt_{0.75}Co_{0.25}$ to 1.57 Å on the Pd surface, the only one qualitatively difference being on Pt (111) (Figure 7.3). On the Pt(111) surface, the hydrogen bond distance was shortened to about 1.39 Å, while the O–H bond distance in the donor molecule was elongated to 1.1 Å, the highest value in all four surfaces. This adsorption was accompanied with a reduction in the water molecule distance from the surface. The geometries in the cases where OH was involved in two hydrogen bonds were very similar on all four surfaces, with a donor bonding distance of 2.1 Å and an acceptor of 1.66 Å.

Table 7.4.

Hydroxyl adsorption energies in the presence and absence of water on transition metal surfaces.

System	ΔE_1 (eV)	O-M dist (Å)	ΔE_2 (eV)	O-M dist (Å)
$Pt_{0.75}Co_{0.25}$-OH	−2.46	2.13	−1.87	2.06
Pt-OH	−2.72	2.13	−2.08	2.02
$Pd_{0.75}Co_{0.25}$-OH	−2.68	2.11	—	—
Pd-OH	−2.88	2.08	−2.17	1.97

ΔE_1 (eV) and ΔE_2 (eV) are in presence of water and in vacuum respectively, O–M is the distance from the oxygen atom of the OH radical to the closest metal atom.

.

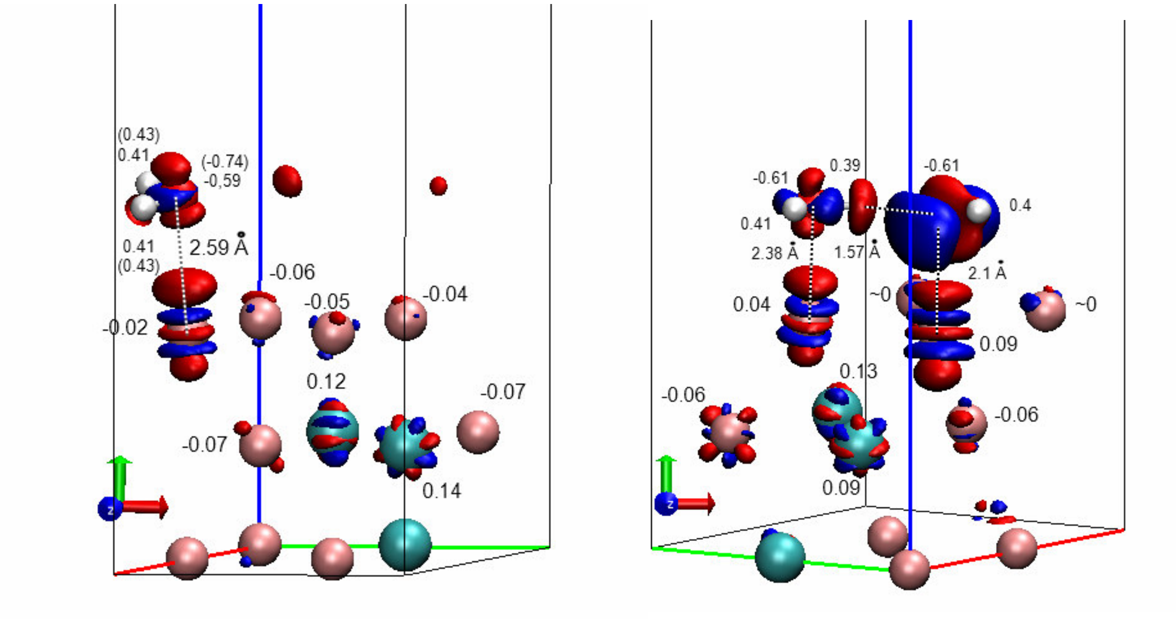

Fig. 7.3. Left: Electron density difference for water (θ=0.25) on the $Pd_{0.75}Co_{0.25}$ surface. Right: Electron density differences for the hydroxyl – water adsorption case. The Lowdin charges for the adsorbates and first two surface layers are also indicated. The numbers between parenthesis corresponds to the charges of the isolated water molecule. The $\Delta\rho$ isosurfaces were fixed at +/– 0.003 $e^{-}/Å^{3}$.

7.2.4. Hydroperoxyl (HO_2)

The calculated values for adsorption energies together with distances and structure show that hydroperoxyl acts as a relatively strong donor and a weaker acceptor in hydrogen bonding. The differences in adsorption energies between hydrated and non hydrated cases lie in between the ones observed for dioxygen and hydroxyl, but are closer to the latter at about 0.4 eV (see Table 7.5). The O–O distance remained nearly constant when compared with the adsorption cases where water was not present, indicating that the O–O bond is not weakened by water. The HO_2 plus the coadsorbed water form a bilayer structure, with the HO_2 adsorbed closer to the surface than in the absence of solvent. The HO_2 radical adsorbed tilted, with the OH group further away from the surface and near an hcp hollow position in all four surfaces. Its angle depended on the surface, being 28.15° on $Pt_{0.75}Co_{0.25}$, 37.9° on Pt, 19.15° on $Pd_{0.75}Co_{0.25}$ and 19.65° on Pd (111). This characteristic was the most distinctive one for this intermediate on the surfaces studied.

Table 7.5.

Adsorption energies for hydroperoxyl in the presence and absence of water on the surface.

System	ΔE_1 (eV)	O-O dist (Å)	ΔE_2 (eV)	O-O dist (Å)
$Pt_{0.75}Co_{0.25}$-HO_2	–1.28	1.44	–0.88	1.44
Pt-HO_2	–1.41	1.42	–1.04	1.43
$Pd_{0.75}Co_{0.25}$-HO_2	–1.41	1.47	–0.97	1.46
Pd-HO_2	–1.62	1.48	–1.22	1.47

ΔE_1 (eV) and ΔE_2 (eV) are in presence of water and in vacuum respectively.

.

7.2.5. Hydrogen Peroxide (H_2O_2)

After placing hydrogen peroxide in its undissociated form with water surrounding it and allowing it to relax, it was found it dissociates to yield two adsorbed hydroxyls as in the case where water was not present. In some of these optimizations the final dissociated hydroxyls were from water after a rearrangement of the bonds during relaxation. The final geometry (see Figure 7.4) included a close hydrogen bonding between one of the hydroxyls and a water molecule with the consequent elongation of the O–H bond inside the donor water molecule (1.08 Å, 1.11 Å, 1.04 Å and 1.05 Å in $Pt_{0.75}Co_{0.25}$ Pt, Pd and $Pd_{0.75}Co_{0.25}$ respectively). At the same time the hydrogen bonding distance to the neighboring hydroxyl decreased, giving 1.39 Å, 1.34 Å, 1.5 Å and 1.48 Å in $Pt_{0.75}Co_{0.25}$, Pt, Pd and $Pd_{0.75}Co_{0.25}$ respectively. The hydroxyls resulting from the hydrogen peroxide dissociation were found at top sites on all surfaces with OH lying more parallel to the surface than in cases where water was not present. Adsorption energies are given in Table 7.6.

Table 7.6. Energies for hydrogen peroxide dissociation per hydroxyl formed in presence and absence of water on the surface.

System	ΔE_1 (eV)	ΔE_2 (eV)
$Pt_{0.75}Co_{0.25}$-2OH	−2.06	−1.67
Pt-2OH	−2.66	−2.06
$Pd_{0.75}Co_{0.25}$-2OH	−2.04	−1.80
Pd-2OH	−2.60	−2.14

ΔE_1 (eV) and ΔE_2 (eV) are in presence of water and in vacuum respectively.

.

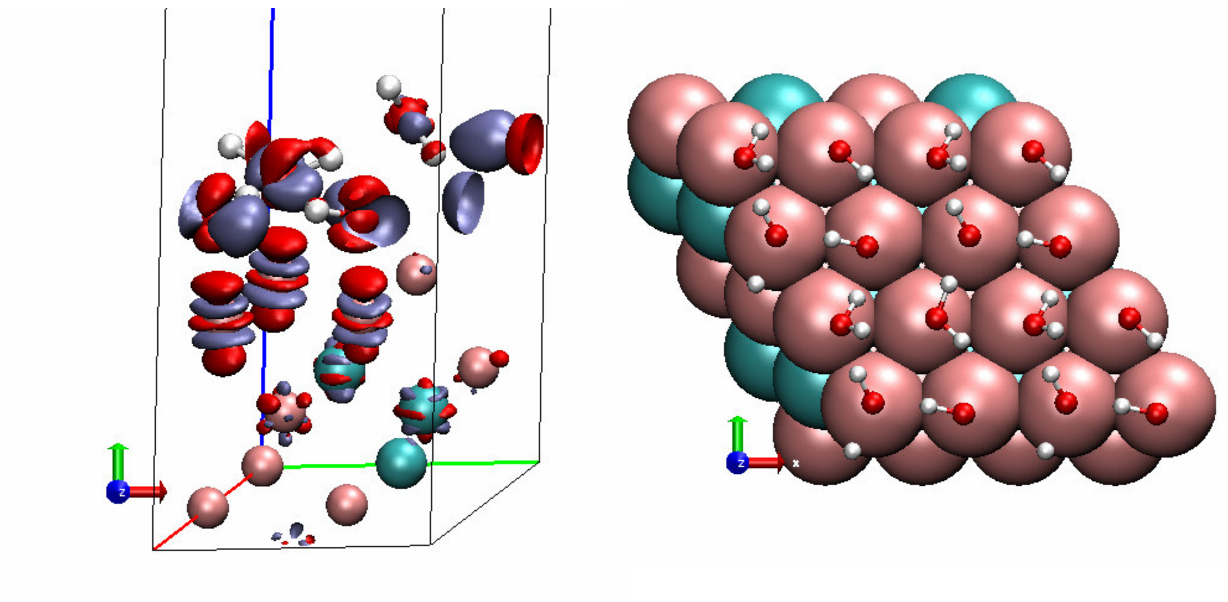

Fig. 7.4. Results of hydrogen peroxide decomposition on the $Pd_{0.75}Co_{0.25}$ surface. The left figure shows the electron density differences at $\Delta\rho = +/- 0.01\ e^{-}/\text{Å}^{3}$. At the right is a four-cell view of the same system.

7.3. Free Energy Profiles

Via generation of free energy profiles, n this section we study two representative mechanisms of the OERR, i.e. one for each pathway. Gibbs free energy changes for the elementary steps including zero point energies and entropies, and cell potential effects are estimated following the methodology introduced by Norskov et al. [63, 64]

The ΔG for the overall reaction was calculated to be 2.13 eV that makes the theoretical results off by about 14% less than the experimental value is 2.5 eV. As already mentioned in Section 6.3 this is attributed in part to the difficulties in modeling the O_2 electronic structure[64]. The results given below introducing the electrode potential into the free energy profiles are based on the *calculated* ΔG for the overall reaction. All free energy profiles were calculated at pH =0.

In this section, we include the presence of water as coadsorbed species on the four metal surfaces and we analyze its influence on the free energy profiles. The effect of the water can be classified into two different types of contributions. One of them is independent of the nature of the surface and is given by the lateral interactions water – adsorbate while the other one is the combined effect of water and the adsorbates on the metal-metal bonding of the surface and subsurface atoms. This effect is surface dependent. The lateral interactions dominate, especially in cases where one or more hydrogen bonds can be generated. Overall the qualitative effect is similar for all four surfaces, with rather small individual differences.

7.3.1. A Direct Pathway Mechanism

The direct mechanism associated with the two electron pathway is the same as that studied in Section 6. The difference now is that the free energy profile is constructed from the adsorption energy tables where the presence of water was explicitly taken into account. The reader is referred to Section 6.3.1 for details of the equations used to estimate the free energies for each step.

$$\frac{1}{2}O_2 + * \rightarrow O* \tag{6.4}$$

$$O* + (H^+ + e^-) \rightarrow OH* \tag{6.5}$$

$$OH* + (H^+ + e^-) \rightarrow H_2O + * \tag{6.6}$$

The main difference observed when water effects are introduced is that because of the lower value of the interaction water-O and the strong hydrogen bonding formed between OH and its neighbor water molecules, the profile predicts that water dissociation is downhill at the cell equilibrium potential in all cases except on $Pd_{0.75}Co_{0.25}$. Another difference on the most active catalyst ($Pt_{0.75}Co_{0.25}$) according to this mechanism, is that the free energy profile at U = 0.78 V is entirely downhill from reactants to products (Figure 7.5). The case where adsorbed oxygen reacts with water to give OH was addressed in Section 7.2.2.

.

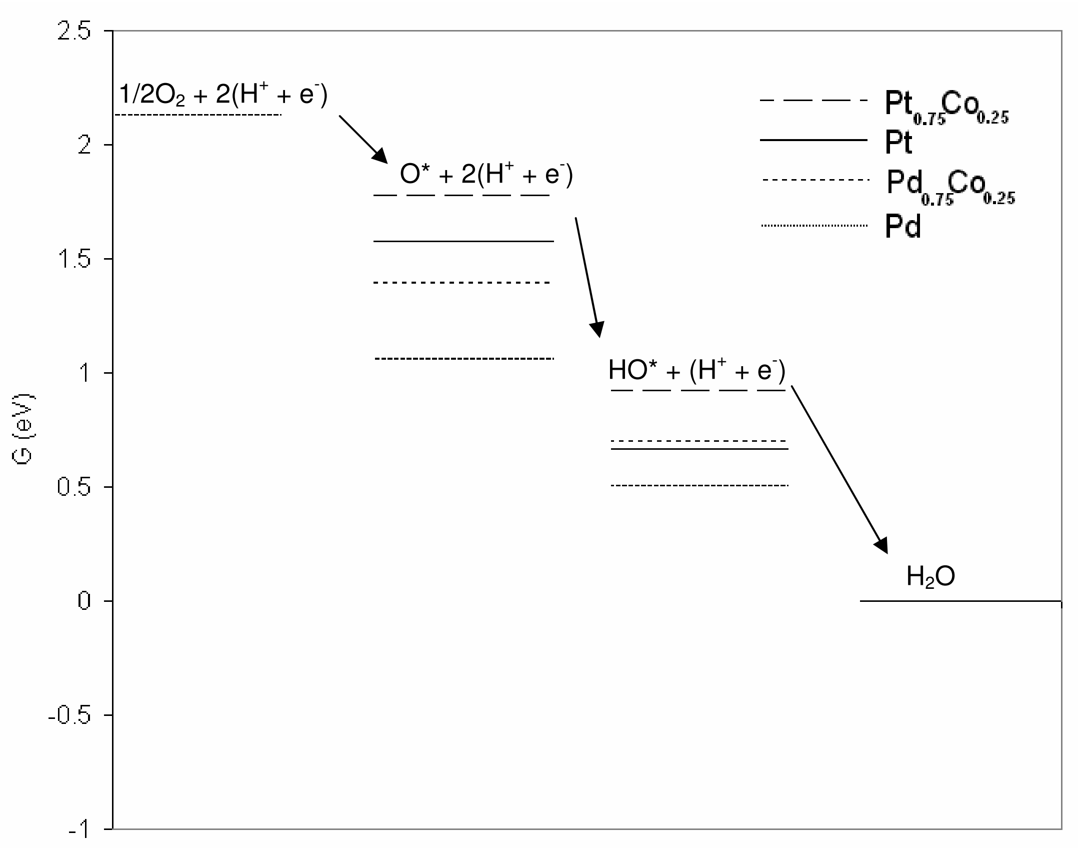

Fig. 7.5. Free energy profile for the series mechanism for the open-circuited cell (U= 0V)

In Figure 7.5 the free energy profile for the open circuited cell (that is U = 0V) is shown, in agreement with already with published findings that the profile is entirely downhill. Indeed, in this case the reaction behaves like in the gas-phase reaction of hydrogen and oxygen to form water, and all the steps are highly exothermic. If we compare this figure with those at other potentials it can be seen that the less exothermic steps are those that will likely become uphill at potentials different from 0 V. This hints at the location of probable “bottleneck” steps in the mechanism.

.

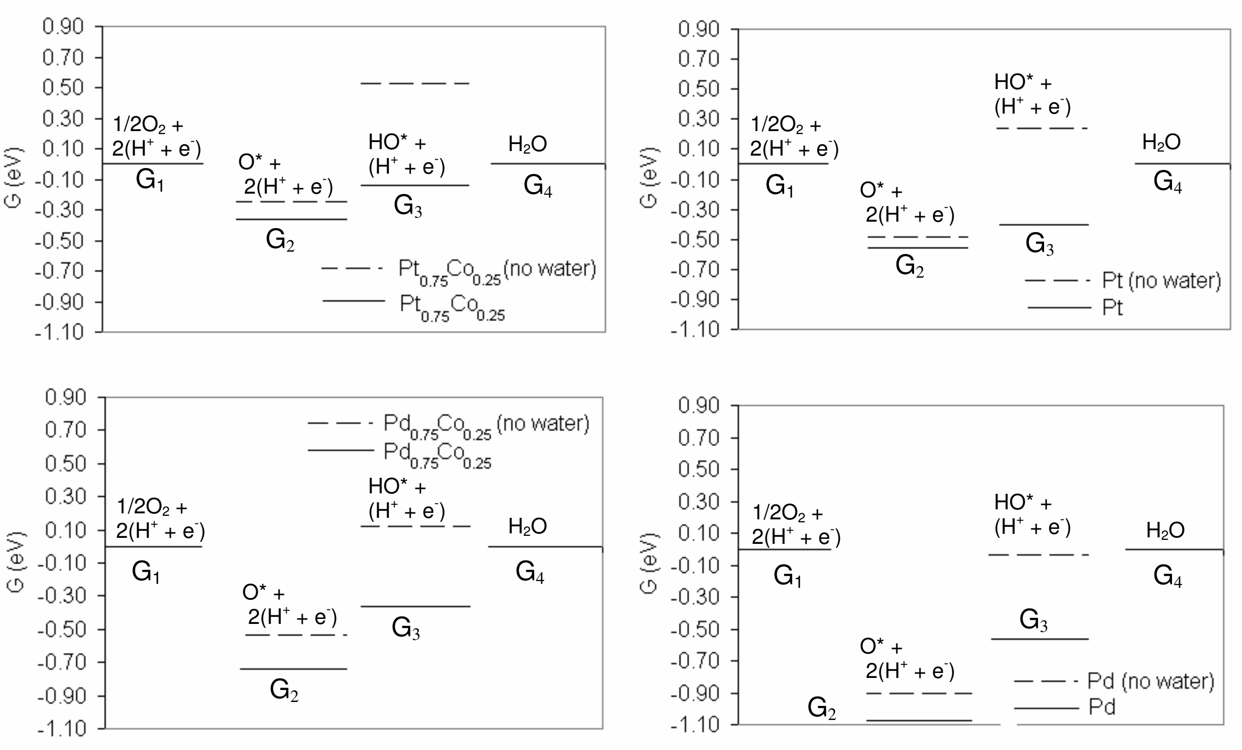

Fig. 7.6. Direct mechanism Gibbs free energy profiles calculated at U= 1.07 V for all studied surfaces with and without water interacting with the intermediates.

Figure 7.6 shows a comparison of the effect of water on the free energy profiles in all four surfaces. As is expected, the added lateral interaction between the adsorbates and water are essentially surface-independent and the effects are therefore similar from one surface to another. The lowering in the hydroxyl energy due to interactions with water also changes the location of the highest thermodynamic barrier for the direct mechanism on platinum from the first to the second protonation. This is common to two of the other three surfaces (Pd and $Pd_{0.75}Co_{0.25}$), while on the $Pt_{0.75}Co_{0.25}$ surface the first protonation is has the highest thermodynamic barrier. This trend follows the location of the d band on the various surfaces, the most reactive having the second protonation as a possible rate-determining step in the direct mechanism, while the least reactive surface has close

.

values for the thermodynamic barriers, with the first protonation being slightly higher than the others.

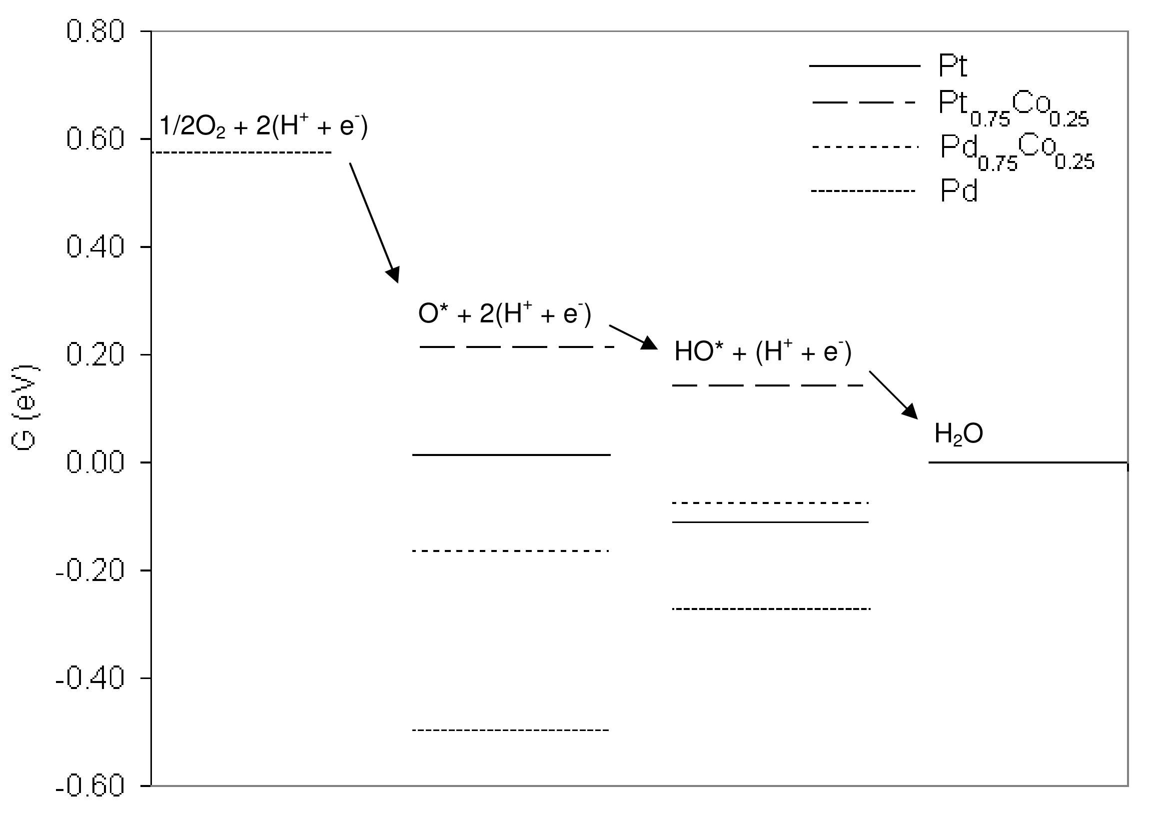

Fig. 7.7. DFT calculated Gibbs free energy profile for a *direct* mechanism of the OERR on Pt, $Pt_{0.75}Co_{0.25}$ and $Pd_{0.75}Co_{0.25}$, and Pd surfaces at U = 0.78 V

At a potential U=0.78 V, close to the nominal fuel cell working potential in the series mechanism and with a coverage on the surface (excluding water) of $\theta = 0.25$ we see in Figure 7.7 that the only profile that is entirely downhill is the one for the $Pt_{0.75}Co_{0.25}$ surface. The uphill barriers are similar in the Pt and $Pd_{0.75}Co_{0.25}$ surfaces and slightly more pronounced on the Pd(111) surface were H_2O dissociation is favorable according to the calculations.

.

7.3.2. A Series Pathway Mechanism

The Gibbs free energy profile for a *series* mechanism indicated by reactions 6.12 through 6.16 is shown in Figure 7.8 at U=0 V. In this mechanism, we assume that H_2O_2 is unstable on all the surfaces, thus the result of the second protonation reaction is its immediate dissociation yielding two adsorbed hydroxide radicals. This assumption is supported by all the geometry optimizations where we found that hydrogen peroxide dissociated when initially placed at a position above the surface close to the optimum observed for its precursor adsorbed hydroperoxyl on all four surfaces.

$$O_2 + * \rightarrow O_2 * \qquad (6.12)$$

$$O_2 * + (H^+ + e^-) \rightarrow HO_2 * \qquad (6.13)$$

$$HO_2 * + (H^+ + e^-) \rightarrow H_2O_2 * \rightarrow 2OH * \qquad (6.14)$$

$$2OH * + (H^+ + e^-) \rightarrow (H_2O + OH) * \qquad (6.15)$$

$$(H_2O + OH) * + (H^+ + e^-) \rightarrow 2H_2O + * \qquad (6.16)$$

The reader is referred to Section 6.3.2 for details of the equations used to estimate the free energies for each step.

.

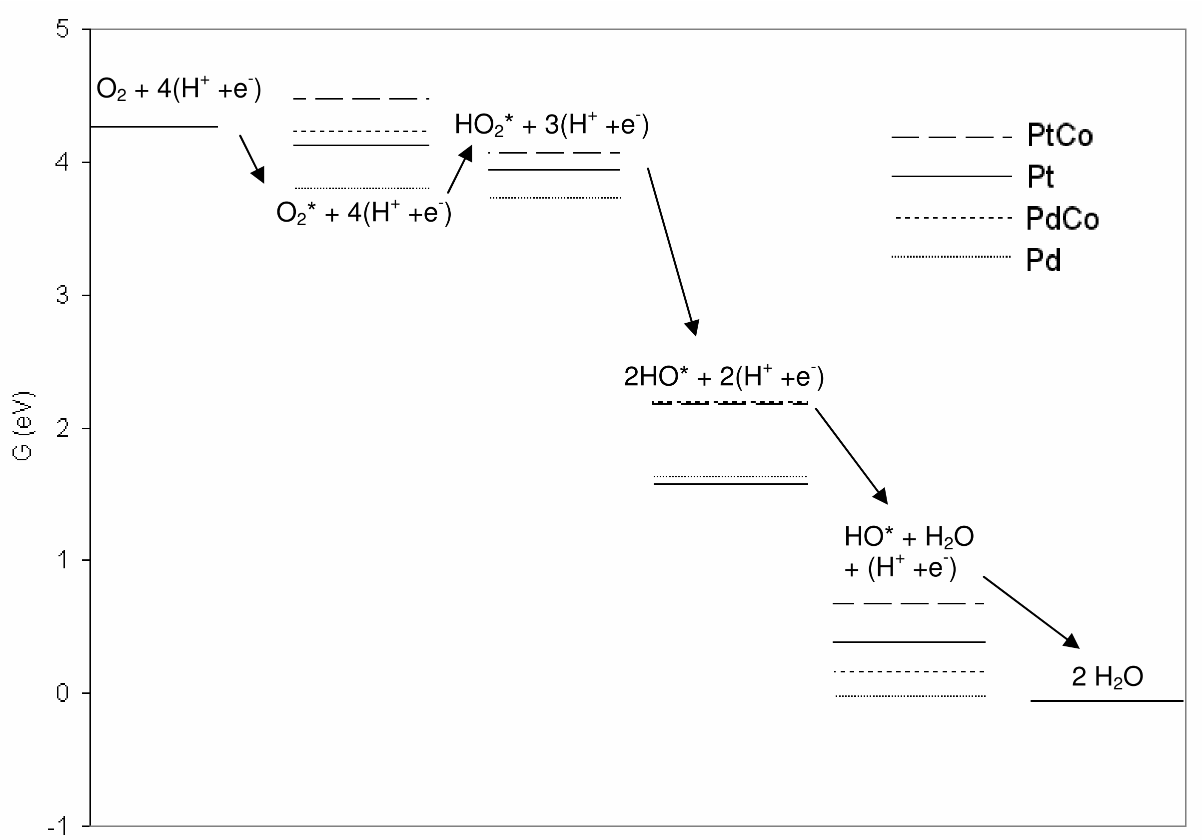

Fig. 7.8. DFT calculated Gibbs free energy profile for a possible *series* mechanism of OERR in Pt, $Pt_{0.75}Co_{0.25}$ and $Pd_{0.75}Co_{0.25}$, and Pd surfaces at U=0 V.

In Figure 7.8 we see the free energy profile at open-circuited cell in the series mechanism (i.e. U = 0 V). Again this corresponds to the gas phase reaction of hydrogen and oxygen to form water. Most of the steps are exothermic, with small activation barriers in the oxygen adsorption case, indicating that the higher barrier at potentials different from U=0 V might be located in the first elementary steps in the mechanism.

.

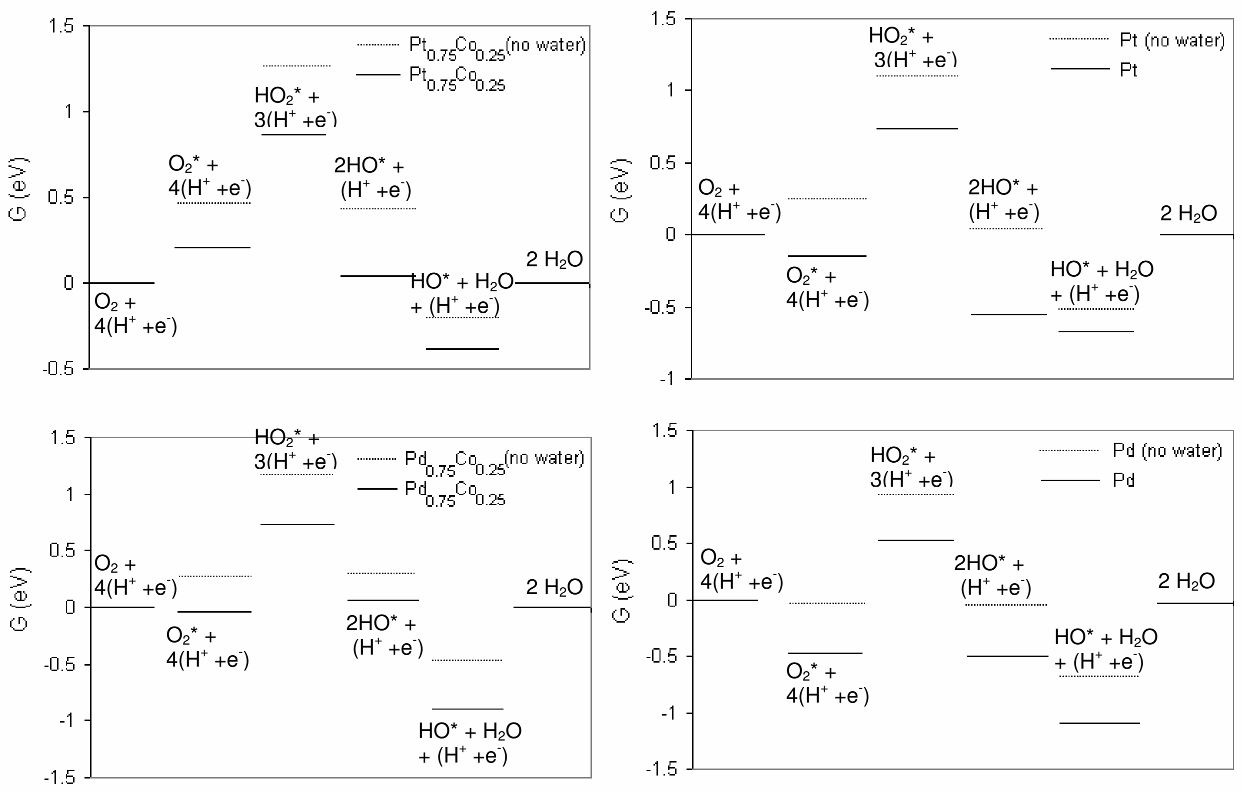

Fig. 7.9. DFT calculated Gibbs free energy profile for a possible *series* mechanism of OERR in Pt, $Pt_{0.75}Co_{0.25}$ and $Pd_{0.75}Co_{0.25}$, and Pd surfaces at U=1.07 V. The cases shown are those where water interactions are included and those where they are neglected.

Figure 7.9 shows the free energy profiles for the four surfaces for the cases when the water was both included and neglected in the calculations. As discussed at the beginning of this section, the effect of water in all four surfaces is qualitatively similar. The location of the highest thermodynamic barrier, thus the most probable location for the rate determining step, is in the first hydrogenation and electron transfer (reaction 6.13). In all surfaces at the cell equilibrium potential, water dissociation on the surfaces is favored, producing OH and H_3O^+ species. This may be compared with simulation

.

results of water layers on Pt(111) surfaces previously describing this type of behavior. At U = 0.78 V (Figure 7.10) the principal features remain the same and the highest barrier is still the first proton transfer in all four surfaces.

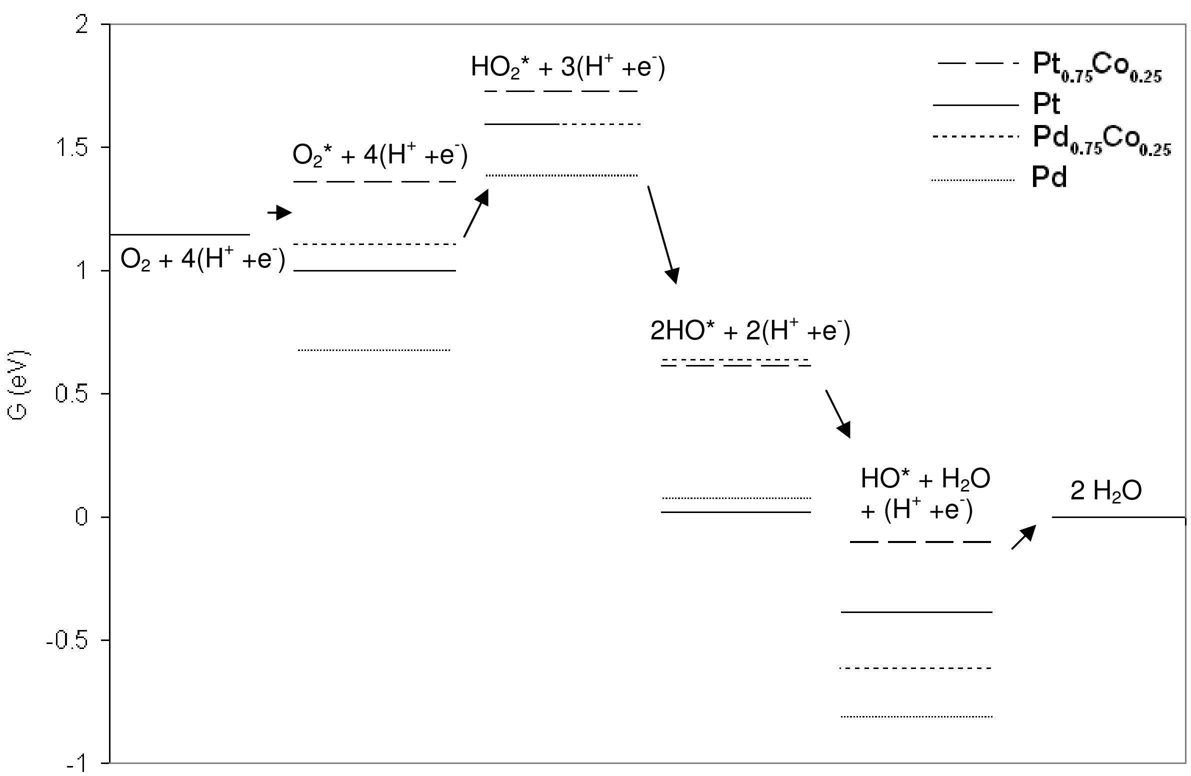

Fig. 7.10. DFT calculated Gibbs free energy profiles for a possible *series* mechanism for the OERR in Pt, $Pt_{0.75}Co_{0.25}$ and $Pd_{0.75}Co_{0.25}$, and Pd surfaces at U=0.78 V. The interaction between water and OERR intermediates was taken into account.

.

At U=0.78 V (Figure 7.10) the resulting profile is very interesting. The highest barrier is for the first proton and electron transfer, which by many authors have considered as the likely rate determining step. The other steps are either downhill or with small barriers. At this potential, the model predicts some water dissociation in all four surfaces with magnitude of the observed downhill barriers (when reading the profile from right to left) ordered according to surface reactivity.

7.4. Conclusions

The calculated free energy profiles and the magnitude of the barriers in both mechanisms are comparable, favoring the hypothesis that both the *direct* and *series* O_2 reduction mechanisms might operate in parallel. On the other hand, experimental observations indicate that the reaction is first order on O_2 and therefore the series pathway should be the active one. The rate determining step should be located before the O–O bond splitting in order to satisfy these observations. This is consistent with our simulations on the individual intermediates on all four surfaces. We found that the O–O bond is strong enough so stable forms of the intermediates can be found being hydrogen peroxide the exception. Also the magnitude of the barriers found in the direct mechanism do not include the activation energy required to dissociate dioxygen and the diffusion barriers

In the *direct* mechanism, the formation of strong hydrogen bonding lowers the energy of some steps in the mechanism changing the location of the highest barrier on three (Pt, Pd and $Pd_{0.75}Co_{0.25}$) of the four surfaces as indicated by the free energy profiles at the cell equilibrium potential. At U = 0.78 V, the only profile that is entirely downhill is the one associated with the $Pt_{0.75}Co_{0.25}$ surface.

In the *series* mechanism, both at U = 0.78 V and 1.07 V, the highest barrier in all cases was the first proton and electron transfer reaction which is the probable rate determining step when this mechanism is active. The behavior of the $Pd_{0.75}Co_{0.25}$ profiles was found to be consistently closer to those observed in Pt and $Pt_{0.75}Co_{0.25}$. This

.

constitutes a good theoretical indication of this alloy as a prospective catalyst for oxygen electroreduction, in accordance with experimental results.

.

8. HYDROGEN PEROXIDE FORMATION AS A SIDE REACTION OF THE OXYGEN ELECTROREDUCTION REACTION

There is nothing more practical than a good theory.
- James Clerk Maxwell

8.1. Introduction

Hydrogen peroxide formation, a possible side reaction in the four electron pathway, is studied in this section. We analyzed free energy profiles for two mechanisms of hydrogen peroxide formation at U=0.78 V and studied the conditions under which its formation will be more favorable on the four surfaces studied. All profiles shown here do not include water-intermediates interactions.

The incomplete reduction of oxygen to form hydrogen peroxide is given by:

$$O_2 + 2 \cdot H + 2e^- \rightarrow H_2O_2 \qquad (8.1)$$

The calculated value for the ΔG for the gas phase reaction was –0.73 eV in good agreement with the experimental value of –0.767 eV[4]. In the following analysis we assume that that the electrode potential is 0.78 V, that is, we assume that the cell is mostly producing water and the potential has not change much from normal working potential range.

8.2. Analysis of Two Possible Mechanisms for Hydrogen Peroxide Formation

The first mechanism involves hydrogen peroxide desorption immediately after the protonation of hydroperoxyl, i.e.:

.

$$O_2 + * \rightarrow O_2 * \qquad (8.2)$$

$$O_2 * + (H^+ + e^-) \rightarrow HO_2 * \qquad (8.3)$$

$$HO_2 * + (H^+ + e^-) \rightarrow H_2O_2 \qquad (8.4)$$

In this case, we assume that instead of dissociating immediately, after the second hydrogenation hydrogen peroxide is formed (Figure 8.1).

The second case studied was by hydroxyl recombination on the surface:

$$O_2 + * \rightarrow O_2 * \qquad (8.5)$$

$$O_2 * + (H^+ + e^-) \rightarrow HO_2 * \qquad (8.6)$$

$$HO_2 * + (H^+ + e^-) \rightarrow 2OH * \qquad (8.7)$$

$$2OH* \rightarrow H_2O_2 \qquad (8.8)$$

In principle, this mechanism appears to be less favorable than the first one. If the hydroperoxyl dissociates immediately after the second protonation, the resulting hydroxyls will bind to the surface with relatively high energy and stabilizing each other by hydrogen bond formation. Thus, recombination to form hydroperoxide seems to be less likely at this point. Analyzing Figure 8.2, we see that this is the case and in all four surfaces there is a large thermodynamic barrier for H_2O_2 formation from two adsorbed hydroxyls at U = 0.78 V.

.

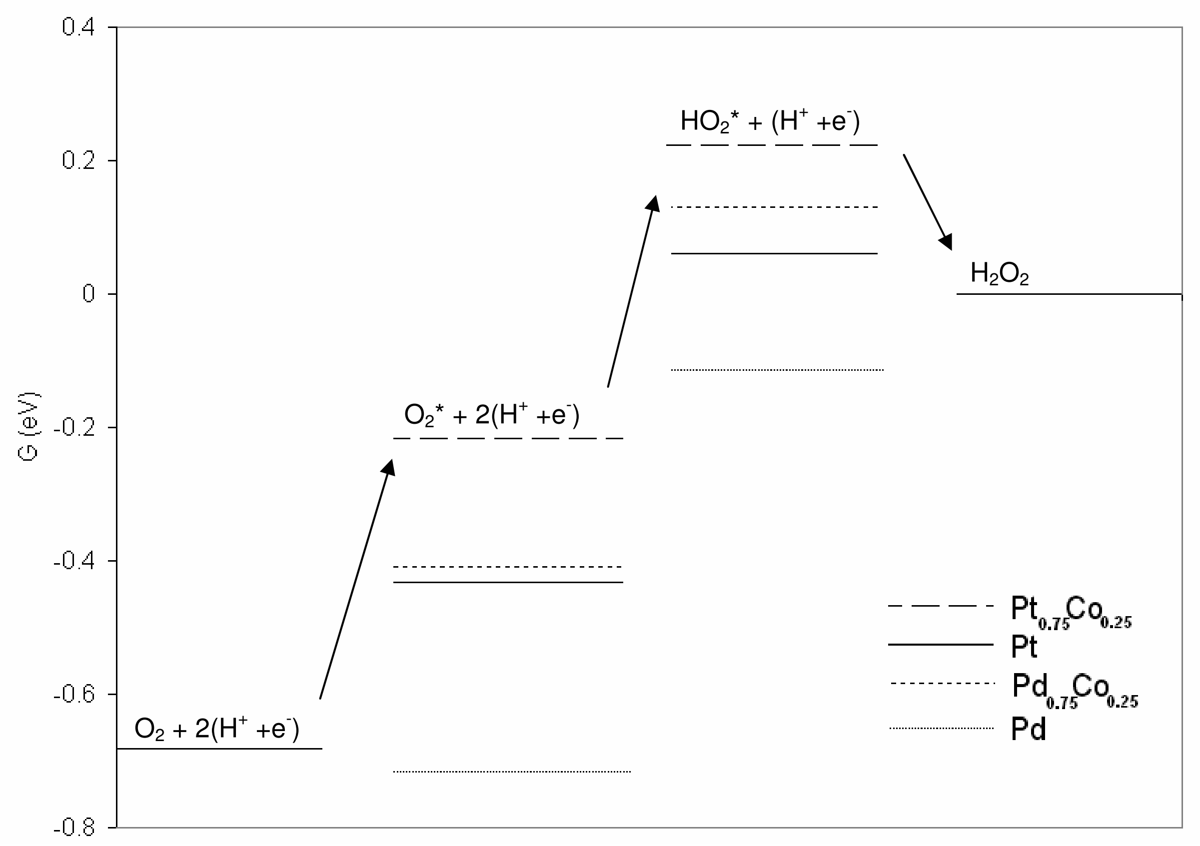

Fig. 8.1. Gibbs free energy profile for a direct mechanism for hydrogen peroxide production in the fuel cell at U =0.78 V.

.

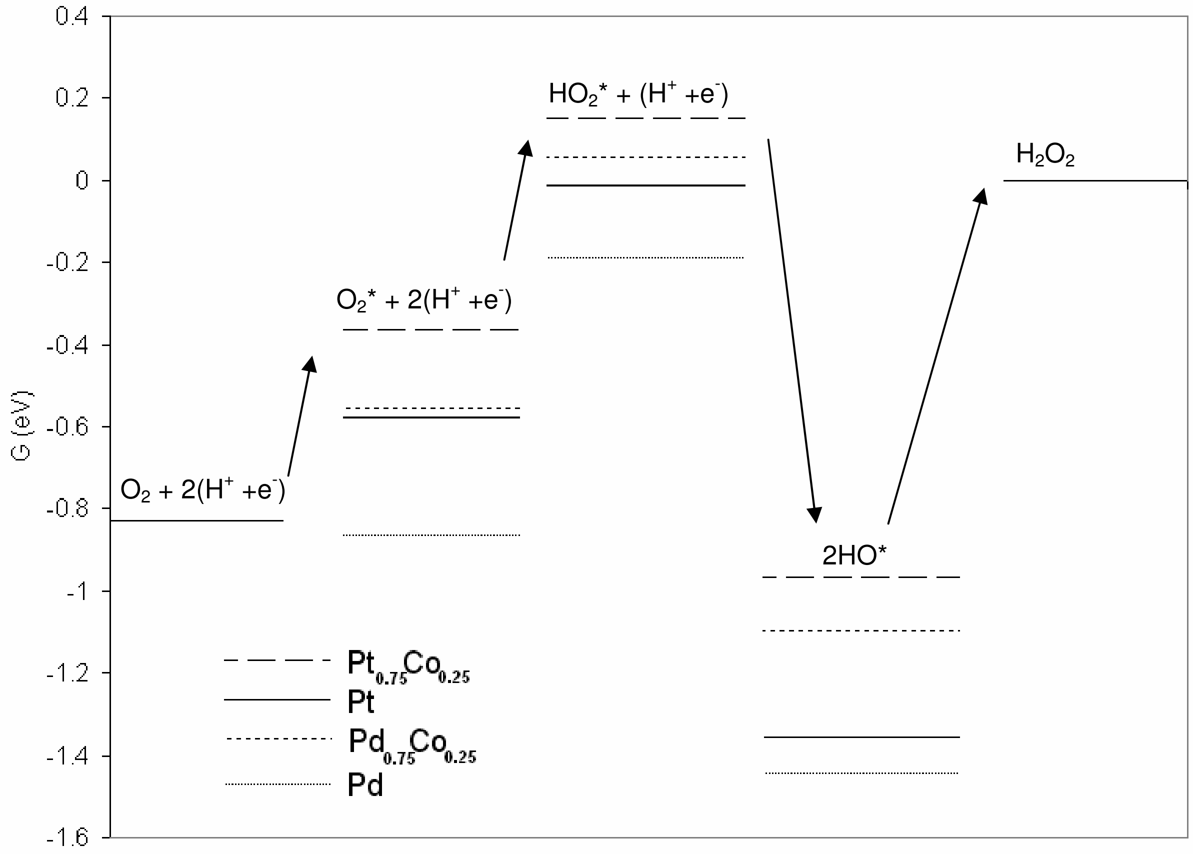

Fig. 8.2. Gibbs free energy profile for an associative mechanism for hydrogen peroxide production in the fuel cell at U =0.78 V.

.

8.3. Conclusions

The formation of hydrogen peroxide via two possible mechanisms on the four surfaces studied was analyzed at the U = 0.78 V. In the first case, we found that there are low barriers for H_2O_2 dissociation in all four surfaces, especially considering the fact that the reference state we took is in the gas phase. In the second case, involves recombination of hydroxyls on the surface. The thermodynamic barrier for this is relatively high in all four surfaces because of the high stability the hydroxyl groups have due to hydrogen bond formation. Both models qualitatively explain the low hydrogen peroxide yield at fuel cell working potentials. The actual case where some hydrogen peroxide is detected in fuel cells might be due to thermal excitations that drive hydroperoxyl away from the surface so that protonation occurs relatively far from the surface or in a position unfavorable for hydroperoxide dissociation.

.

9. SUMMARY AND CONCLUSIONS

> Ignorance more frequently begets confidence than does
> knowledge: it is those who know little, not those who know
> much, who so positively assert that this or that problem will
> never be solved by science
> - Charles Darwin

We are in a very exciting period for the evolution of computational physics, with an increasing widening of its applications and reach. The level of development of the theoretical techniques, together with the advancement in hardware and parallel algorithms are giving the researcher increasingly sophisticated tools, allowing the simulation of systems that were out of reach just a few years ago. Nevertheless, the dream of computational laboratory, to be completely independent of experimental observations, is still a goal rather than a reality. The limitations are rooted in the deficiencies in available theories and with their computational costs. Some of these limitations have been mentioned in the introduction, for example, the impossibility of density functional theory to describe highly correlated systems, (e.g., in lanthanides where the f shell is partially filled)[93], long range Van der Waals interactions and band gaps. For more specific examples, we can also mention a recent discussion about the incorrect preferred adsorption site for CO adsorption on transition metals[1-3], problems describing π stacking, and also its failure to predict the correct band structure of Mott insulators as, for example, in the FeO case and others.

In this work, we have analyzed the oxygen electroreduction reaction from a theoretical perspective on different transition metal surfaces. The candidate surfaces were chosen according the Sabatier principle, which says that a good catalyst is one that interacts strongly enough with the reactants to activate them favoring the production of intermediates (i.e. breaking reactants bonds) but with a strength that is below the required to form stable components on the catalyst surface (thus favoring the subsequent bond recombination to form the products). In transition metal surfaces, the result of years of research has established the position of the d-band center as the key variable for

.

the characterization of the surface reactivity. The closer the d band center is to the Fermi level, the more reactive the surface will be. Different variables can change the position of the d band center, some of them are entangled like the lattice constant and the alloy composition. As shown in Section 5.2, Pt and Pd alloys with Co are characterized by contraction in their lattice constants when compared with the pure metals. A change in the lattice constant will also trigger a change in lattice constant in reciprocal space, which is related by $2\pi/a$ to the lattice constant in direct space. This will change the band structure and consequently the electronic properties of the material. Of course, the band structure will also be affected by the chemical interactions of the alloy components. The possibilities for using different compositions and "tuning" catalyst activity are therefore large. Benchmark materials are available from the broad range of available experimental data. The first example is the Pt (111) surface representing the most frequently used pure metal catalyst for oxygen electroreduction. Experimental work has shown that some Pt alloys, for example those with Fe, and Co have enhanced activity when compared with pure platinum. The analysis of the d band centers and the comparison between these alloys and pure platinum may provide a direction in which to move when designing new electrocatalysts.

The interaction of oxygen electroreduction intermediates with different transition metal surfaces has been characterized from different perspectives, from the electronic structure viewpoint via the changes on electron density upon adsorption. This allowed us to obtain a qualitative picture of the electron flow caused by the surface adsorbate interactions. In all cases, we noted slight electron depletion in the dz^2 orbital common to all metal studied and in the dioxygen species a weakening in the O–O bond indicated by a lowering in electron density in the region between the oxygen atoms. The added stability that the proton addition confers to the oxygen was also demonstrated by less dramatic changes in electron densities at the same isosurface levels, as shown by comparison for example of the isosurfaces for oxygen and hydroxyl in Figure 6.1. The description of the interactions from an electronic perspective can also be made by localizing the electrons via a projection of the plane wave expansion into pseudo atomic

.

orbitals followed by a charge population analysis. This analysis was made in Section 5.3 to study the clean $Pd_{0.75}Co_{0.25}$ alloy. In Sections 7.2.2 and 7.2.3 we used the same methodology to quantify charge transfers from adsorbed H_2O, O_2 and OH to the transition metal surfaces. In those cases where strong interactions with oxygen containing species occurred, we found charge transfer from the surface to the intermediates leaving a slight positive charge on the surface. While in the case of the interactions between pure water and the surface the opposite trend was observed.

Adsorption energies for the intermediates of oxygen electroreduction were calculated, both in presence and absence of water. We verified the d-band model and in general found that the strengths of the surface adsorbate bonds were in ascending order: $Pt_{0.75}Co_{0.25} > Pt > Pd_{0.75}Co_{0.25} > Pd$. This follows the same trend as the distance between the d-band and the Fermi level. In molecular dioxygen we verified the presence of different adsorbed molecular precursors and the location of preferred adsorption sites for atomic oxygen and hydroxyl and hydroperoxyl.

In general, it was found from geometry optimization calculations that the O–O bond in the transition metal surfaces is relatively stable up to the second protonation, when it dissociated easily to form two adsorbed hydroxyls on the surface. The interactions between hydroxyls are greatly stabilized due to hydrogen bonding. This is also observed for hydroperoxyl when water is present in the system. This relatively high stability of the O–O bond up to the second protonation is consistent with the experimentally observed kinetic order for OERR.

In the absence of water, the study of the free energy profiles and the magnitude of the thermodynamic barriers for both direct and series mechanisms seem to favor the hypothesis that in O_2 reduction to water both may operate in *parallel*. The highest thermodynamic barriers appear to be located in the first protonation for both mechanisms when the system is studied under conditions of ¼ of a monolayer of adsorbate and in the absence of water. At $U = 0.78$ V the only catalyst that shows an entirely downhill path in the series reaction is $Pt_{0.75}Co_{0.25}$. This hints at why this might be the most active among the four here studied.

.

Water bonds weakly to the different transition metal surfaces studied here, and the range of adsorption energies between surfaces is low. On the other hand, the interaction with adsorbates where hydrogen bonding is possible is strong, stabilizing these intermediates on the different surfaces. In the series mechanism, this changes the free energies thus altering the location of the maximum thermodynamic barrier that is switched from the first to the second protonation. As it was seen in the analysis in Sections 7.3.1 and 7.3.2 these changes are similar on each surface, since lateral interactions are relatively surface independent.

Summarizing the results at the highest level of theory used in this work, the highest barrier in the direct (2 e^- pathway) mechanism was found to be the second proton transfer. Since the second protonation in this mechanism occurs after the O–O bond splitting we are left with two choices to satisfy the observed first order rate on dioxygen for this reaction. The first possibility is that the RDS before dioxygen dissociation and associated with a high activation energy that was not included in the calculation of the profiles. The second possibility is that the series mechanism is not active. In the series (4 e^- pathway) the highest barrier is still located at the first proton and charge transfer on all four catalytic surfaces. This is in good agreement with observed rate laws for this reaction. In presence of bulk water some water dissociation is possible on all studied surfaces (at $U = 0.78$ V), but further dissociation faces a relatively high barrier. The instability of hydrogen peroxide on all surfaces, especially compared with the relatively higher stability of other intermediates, strongly points at this intermediate as the most likely point where the oxygen bond is broken during oxygen reduction. This adds to the argument that this path might be active during oxygen electroreduction.

Formation of hydrogen peroxide, an important side reaction associated with oxygen electroreduction, was studied on all four surfaces. In the first mechanism, the model predicts low thermodynamic barriers (less than 0.2 eV) for hydrogen peroxide dissociation on all four surfaces, with no barrier on Pd (111). In the second possible mechanism, which considers the highly stable adsorbed hydroxyl species as intermediates, hydrogen peroxide is highly unstable.

The future research might include re-visiting the above problems with increased accuracy, for example by using new hybrid functionals that incorporate the exact exchange term. Research is still required on the details of each of the elementary steps, for example, accurate estimation of activation energies in the presence of water. The application and improvement of new algorithms for Ab Initio molecular dynamics is also necessary. For example, modified Lagrangian and other methods for accelerated dynamics to follow and characterize each elementary reaction in a single simulation without getting “trapped” in local minima are also desirable. In all cases, the goal is the complete characterization of the OERR based on Ab Initio tools and the subsequent bridging of microscopic and macroscopic worlds through statistical mechanics.

Finally, new alloys can be tested, for example ternary and quaternary transition metal alloys with no Pt, with the objective of finding compositions with better activity and stability under the challenging fuel cell conditions. The search of new catalysts does not have to be limited to transition metal alloys. Among alternatives that have attracted attention we can mention metalloporphyrins. In fact, the development of non-precious metal catalysts for oxygen reduction is essential for cost effective and therefore commercially viable fuel cells.

.

REFERENCES

[1] P. J. Feibelman, B. Hammer, J. K. Norskov, F. Wagner, M. Scheffler, R. Stumpf, R. Watwe, and J. Dumesic, J. Phys. Chem. B 105 (2001) 4018.

[2] I. Grinberg, Y. Yourdshahyan, and A. M. Rappe, Journal of Chemical Physics 117 (2002) 2264.

[3] R. A. Olsen, P. H. T. Philipsen, and E. J. Baerends, Journal of Chemical Physics 119 (2003) 4522.

[4] National Institute of Standards and Technology, http://srdata.nist.gov/cccbdb/ (2005).

[5] N. C. Handy, Y. Yamaguchi, and H. F. Schaefer, Journal of Chemical Physics 84 (1986) 4481.

[6] L. J. Butler, Annual Rev. Phys. Chem. 49 (1998) 125.

[7] J. M. Thijssen, Computational Physics, Cambridge University Press, Cambridge, UK. (1999). p. 564

[8] Burke K., The ABC of DFT, http://dft.rutgers.edu/kieron/beta/, (2001).

[9] W. Kohn and L. J. Sham, Physical Review 140 (1965) A1133.

[10] P. Hohenberg and W. Kohn, Physical Review 136 (1964) B864.

[11] A. Szabo and N. S. Ostlund, Modern Quantum Chemistry, Dover, New York (1982). p. 480

[12] N. W. Ashcroft and N. D. Mermin, Solid State Physics, Brooks/Cole, Belmont, MA, (1976). p. 848

[13] M. P. Marder, Condensed Matter Physics, Wiley Interscience, New York (2000). p.928

[14] J. P. Perdew and K. Burke, International Journal of Quantum Chemistry 57 (1996) 309.

[15] J. P. Perdew, K. Burke, and M. Ernzerhof, in: Chemical Applications of Density Functional Theory, eds. B. B. Laird, R. Ross, and T. Ziegler, ACS Symposium Series 629, ACS Books, Washington DC, 1996, pp. 453-462

.

[16] W. Koch and M. C. Holthausen, A Chemist's Guide to Density Functional Theory, Wiley-VCH, New York (2001). p. 528

[17] R. M. Martin, Electronic Structure. Basic Theory and Practical Methods, Cambridge University Press, Cambridge, UK. (2004). p. 648

[18] R. Carbó-Dorca, Adv. Quantum Chem. 49 (2005) 121.

[19] H. J. Monkhorst and J. D. Pack, Physical Review B 13 (1976) 5188

[20] D. R. Hamann, M. Schluter, and C. Chiang, Physical Review Letters 43 (1979) 1494.

[21] D. Vanderbilt, Physical Review B 41 (1990) 7892.

[22] A. J. Appleby, Catalysis Review 4 (1970) 221.

[23] J. P. Collman, P. S. Wagenknecht, and J. E. Hutchison, Angew. Chem. Int. Ed. 33 (1994) 1537.

[24] H. S. Wroblowa, Y.-C. Pan, and G. Razumney, J. Electroanal. Chem. 69 (1976) 195.

[25] N. M. Markovic, T. J. Schmidt, V. Stamenkovic, and P. N. Ross, Fuel Cells 1 (2001) 105.

[26] A. Damjanovic and V. Brusic, Electrochim. Acta 12 (1967) 615.

[27] A. J. Appleby, Catalysis Reviews 4 (1970) 221.

[28] E. B. Yeager, Electrochimica Acta 29 (1984) 1527.

[29] S. Mukerjee and S. Srinivasam, Journal of Electroanalytical Chemistry 357 (1993) 201.

[30] S. Mukerjee, S. Srinivasam, M. P. Soriaga, and J. McBeen, Journal of the Electrochemical Society 142 (1995) 1409.

[31] B. N. Grgur, N. M. Markovic, and P. N. Ross, Canadian Journal of Chemistry 75 (1997) 1465

[32] T. Toda, H. Igarashi, H. Uchida, and M. Watanabe, Journal of the Electrochemical Society 146 (1999) 3750.

.

[33] U. A. Paulus, A. Wokaum, G. G. Scherer, T. J. Schmidt, V. Stamenkovic, N. M. Markovic, and P. N. Ross, Electrochimica Acta 47 (2002) 3787.

[34] L. D. Burke and J. K. Casey, Journal of the Electrochemical Society 140 (1993) 1284.

[35] J. L. Fernandez, V. Raghuveer, A. Manthiram, and A. J. Bard, Journal of the American Chemical Society 127 (2005) 13100.

[36] V. Raghuveer, A. Manthiram, and A. J. Bard, Journal of Physical Chemistry B 109 (2005) 22909.

[37] K. Lee, O. Savadogo, A. Ishihara, S. Mitsushima, N. Kamiya, and K. Ota, Journal of the Electrochemical Society 153 (2006) A20.

[38] R. Hoffmann, Angew. Chem. Int. Ed. Engl. 26 (1987) 846.

[39] R. Hoffmann, Review of Modern Physics 60 (1988) 601.

[40] B. Hammer and J. K. Norskov, Surf. Sci 343 (1995) 211.

[41] J. Greeley, J. K. Norskov, and M. Mavrikakis, Annual Rev. Phys. Chem. 53 (2002) 319.

[42] J. K. Norskov, T. Bligaard, A. Logadottir, S. Bahn, L. B. Hansen, M. Bollinger, H. Bengaard, B. Hammer, Z. Sljivancanin, M. Mavrikakis, Y. Xu, S. Dahl, and C. J. H. Jacobsen, Journal of Catalysis 209 (2002) 275.

[43] J. Zhang, M. B. Vukmirovic, Y. Xu, M. Mavrikakis, and R. Adzic, Angew. Chem. Int. Ed. 44 (2005) 2132.

[44] J. Greeley and J. K. Norskov, Surface Science 592 (2005) 104.

[45] P. J. Feibelman, S. Esch, and T. Michely, Phys. Rev. Lett. 77 (1996) 2257.

[46] P. J. Feibelman, Physical Review B 56 (1997) 10532.

[47] A. Bogicevic, J. Stromquist, and B. I. Lundqvist, Phys. Rev. B 57 (1998) R4289

[48] T. Jacob, R. P. Muller, and W. A. Goddard III, J. Phys. Chem. B 107 (2003) 9465.

[49] A. Eichler and J. Hafner, Physical Review B 59 (1999) 5960.

.

[50] A. Eichler, F. Mittendorfer, and J. Hafner, Physical Review B 62 (2000) 4744.

[51] A. Grob, A. Eichler, J. Hafner, M. J. Mehl, and D. A. Papaconstantopoulos, Surf. Sci. 539 (2003) L542.

[52] M. L. Bocquet, J. Cerdá, and P. Sautet, Physical Review B 59 (1999) 15437.

[53] Y. Xu, A. Ruban, and M. Mavrikakis, J. Am. Chem. Soc. 126 (2004) 4717.

[54] A. Michaelides and P. Hua, Journal of Chemical Physics 114 (2001) 513.

[55] J. Roques and A. B. Anderson, Journal of the Electrochemical Society 151 (2004) E85.

[56] H. Ogasawara, B. Brena, D. Nordlund, M. Nyberg, A. Pelmenschikov, L. G. M. Pettersson, and A. Nilsson, Physical Review Letters 89 (2002) 148302.

[57] P. J. Feibelman, Physical Review Letters 91 (2003) 059601.

[58] G. Held, C. Clay, S. D. Barret, S. Haq, and A. Hodgson, The Journal of Chemical Physics 123 (2005) 064711.

[59] G. S. Karlberg, F. E. Olsson, M. Persson, and G. Wahnstrom, Journal of Chemical Physics 119 (2003) 4865.

[60] A. B. Anderson and T. V. Albu, J. Electrochem. Soc. 147 (2000) 4229.

[61] A. Panchenko, M. T. M. Koper, T. E. Shubina, S. D. Mitchell, and E. Roduner, Journal of the Electrochemical Society 151 (2004) A2016.

[62] M. T. M. Koper and R. A. v. Santen, Journal of Electroanalytical Chemistry 472 (1999) 126.

[63] J. K. Norskov, J. Rossmeisl, A. Logadottir, and L. Lindqvist, J. Phys. Chem. B 108 (2004) 17886.

[64] J. Rossmeisl, A. Logadottir, and J. K. Norskov, Chemical Physics 319 (2005) 178.

[65] B. Hammer, L. B. Hansen, and J. K. Norskov, Physical Review B 59 (1999) 7413.

[66] A. Alavi, P. Hu, T. Deutsch, P. L. Silvestrelli, and J. Hutter, Physical Review Letters 80 (1998) 3650.

.

[67] A. Kokalj, A. Lesar, M. Hodoscek, and M. Causa, J. Phys. Chem. B 103 (1999) 7222.

[68] A. Kokalj and M. Cesna, J. Phys.: Condens. Matter 11 (1999) 7463.

[69] Vanderbilt Ultra-Soft Pseudopotential Site. http://www.physics.rutgers.edu/~dhv/uspp/ (2007)

[70] N. Marzari, D. Vanderbilt, A. De Vita, and M. C. Payne, Physical Review Letters 82 (1999) 3296.

[71] C. G. Broyden, J. of the Inst. for Math. and Applications 6 (1970) 222.

[72] R. Fletcher, Mathematics of Computation 24 (1970) 317.

[73] D. Goldfarb, Mathematics of Computation 24 (1970) 647.

[74] D. F. Shanno, Mathematics of Computation 24 (1970) 647.

[75] S. Scandolo, P. Giannozzi, C. Cavazzoni, S. de Gironcoli, A. Pasquarello, and S. Baroni, Z. Kristallogr. 220 (2005) 574.

[76] W. Humphrey, A. Dalke, and K. Schulten, J. Molec. Graphics 14 (1996) 33.

[77] A. Kokalj, Computational Materials Science 28 (2003) 155.

[78] R. M. Wentzcovitch, J. L. Martins, and G. D. Price, Physical Review Letters 70 (1993) 3947.

[79] A. Koote, C. Haas, and R. A. de Groot, Journal of Physics: Condensed Matter 3 (1991) 1133.

[80] T. Tohyama, Y. Ohta, and M. Shimizu, Journal of Physics: Condensed Matter 1 (1989) 1789.

[81] J. W. Taylor, J. A. Duffy, J. Poulter, A. M. Bebb, M. J. Cooper, J. E. McCarthy, D. N. Timms, J. B. Staunton, F. Itoh, H. Sakurai, and B. L. Ahuja, Physical Review B 65 (2001) 024442-1.

[82] M. D. Segall, R. Shah, C. J. Pickard, and M. C. Payne, Physical Review B 54 (1996) 16317.

[83] D. Sanchez-Portal, E. Artacho, and J. M. Soler, Solid State Communications 95 (1995) 685.

.

[84] V. Stamenkovic, T. J. Schmidt, P. N. Ross, and N. M. Markovic, Journal of Electroanalytical Chemistry 554-555 (2003) 191.

[85] O. Savadogo, K. Lee, K. Oishi, S. Mitsushima, N. Kamiya, and K.-I. Ota, Electrochem. Comm. 6 (2004) 105.

[86] M. H. Shao, K. Sasaki, and R. R. Adzic, Journal of the American Chemical Society 128 (2006) 3526.

[87] J. L. Fernandez, D. A. Walsh, and A. J. Bard, J. Am Chem. Soc. 127 (2005) 357.

[88] A. Eichler and J. Hafner, Physical Review Letters 79 (1997) 4481.

[89] C. Puglia, A. Nilsson, B. Hernnas, O. Karis, P. Bennich, and N. Martensson, Surf. Sci. 342 (1995) 119.

[90] S. J. Suresh and V. M. Naik, Journal of Chemical Physics 113 (2000) 9727.

[91] S. Meng, E. G. Wang, and S. Gao, Physical Review B 69 (2004) 195404.

[92] E. J. Lamas and P. B. Balbuena, Journal of Chemical Theory and Computation 2 (2006) 1388.

[93] A. Grob, Surf. Sci. 500 (2002) 347.

.

VITA

Eduardo J. Lamas received his B.S. degree in chemical engineering from the University of Buenos Aires in January of 1999. He worked as a research assistant at INGAR, a chemical engineering research institute in Santa Fe, Argentina in fault detection and diagnosis in chemical processes from 1999 to 2001. In 2001, he started his Ph.D. program at the University of South Carolina and later transferred to Texas A&M where he got his Ph.D. degree in chemical engineering in May 2007.

Mr. Lamas may be reached at 620 Jack E. Brown Engineering Building 3122 TAMU, College Station, TX 77843-3122. His e-mail address is: eduardo.j.lamas@gmail.com.

.